

A Physical Model for the Spectral-Timing Properties of Accreting Black Holes

Ra'ad D. Mahmoud¹^{*} & Chris Done¹

¹*Department of Physics, University of Durham, South Road, Durham DH1 3LE*

Accepted XXX. Received YYY; in original form ZZZ

ABSTRACT

The rapid X-ray variability of black hole accretion flows in the low/hard state has a strong energy dependence, even looking only above 3 keV where the emission is dominated by Comptonisation. This is clear from the different shapes of the power spectra at different energies, and in the complex pattern of the time lags between distinct energy bands. Our analytic technique fits the energy-dependent power spectra and time lags using a physical model based on fluctuations propagating through a spectrally inhomogeneous flow. The spectral components are set by jointly fitting to the time averaged and Fourier resolved spectra.

This framework simultaneously approximates the energy spectra, power spectra in different energy bands and time lags between bands from high quality Cygnus X-1 data where clear structure in the timing statistics is present. We find that the model features demanded by the data are (1) enhanced variability and emission at key radii within the flow, (2) destruction of propagating fluctuations near positions of enhanced turbulence/emission, and (3), stratification of the Comptonising flow into at least three regions, each producing a distinct Compton component. These results establish the importance of specific radii in the Comptonising zone, likely associated with the disc truncation, the inner edge of the flow, and/or the jet launch radius.

Key words: accretion, accretion discs – X-rays: binaries – X-rays: individual: Cygnus X-1

1 INTRODUCTION

The overall spectral properties of the low/hard state in black hole binaries (BHBs) are often interpreted in a truncated disc/hot inner flow geometry (see e.g. the review by Done, Gierliński & Kubota 2007; hereafter DGK07). In this picture, a cool, optically thick, geometrically thin disc (Shakura & Sunyaev 1973) transitions at some radius to a hot, optically thin, geometrically thick inner flow which behaves similarly to an advection-dominated accretion flow (ADAF, Narayan & Yi 1995). A decreasing truncation radius between the cool, truncated disc and the hot, inner flow as the mass accretion rate increases (on timescales of days to weeks) leads to stronger disc emission, and hence stronger Compton cooling of the hot flow, so that its spectrum steepens. This also provides a mechanism to explain the transition to the disc-dominated state when the truncated disc finally reaches the innermost stable circular orbit (ISCO; Esin, McClintock & Narayan 1997; DGK07).

More recent work has shown in detail how this can also

explain the properties of the fast variability (on timescales of 0.01 – 10 s), including the strong low frequency quasi-periodic oscillation (QPO). The radius of the thin truncated disc sets the outer radius of the hot inner flow. Any turbulence in the hot flow will have a timescale which decreases with radius, so the longest timescale fast variability is set by the outer radius of the hot flow (Lyubarskii 1997; Arévalo & Uttley 2006); this defines the low-frequency break in the power spectrum. The QPO can be produced in the same geometry by Lense-Thirring (relativistic vertical) precession of the entire hot flow (Fragile et al. 2007; Ingram et al. 2009), predicting that the iron line centroid energy is modulated on the same quasi-period as the QPO in the case of the BHB H1743-322, as shown by the data (3.8 σ detection; Ingram et al. 2016). The decrease in truncation radius with increasing mass accretion rate therefore drives a correlated decrease in the power spectral break timescale, and a decrease in the QPO timescale as the Compton spectrum softens (Wijnands & van der Klis 1999; Klein-Wolt & van der Klis 2008; Ingram & Done 2012b).

This geometry also offers a qualitative explanation of the more complex, higher order variability properties. It

^{*} E-mail: ra'ad.d.mahmoud@durham.ac.uk

is well established that BHB lightcurves on fast timescales show variability in higher energy bands lagging behind that from lower energy bands (Miyamoto & Kitamoto 1989; Nowak et al. 1999; Grinberg et al. 2014). These lags might be expected in a model where the low energy band is dominated by the disc, and the high energy band is dominated by Comptonisation from the hot flow. Fluctuations in the disc will propagate inwards down through the hot flow, but with some lag time (Uttley et al. 2014; Rapisarda et al. 2016). However, such models fundamentally do not explain why these lags are seen between bands where the disc emission is negligible, nor why the lags also depend on the frequency of variability (Nowak et al. 1999; De Marco et al. 2015; Misra et al. 2017). Instead these can be explained if the hot flow is stratified not only in variability timescale, but also in spectral shape, such that the outer regions of the flow are associated with softer Compton spectra than the inner regions (Kotov, Churazov & Gilfanov 2001; Gierliński, Done & Page 2009). Slow variability is therefore generated at the largest radii, in the region where the Compton spectrum is softer. These fluctuations have the largest distance to travel (i.e. the longest lag time) before they modulate the hardest spectral inner regions, while faster variability is produced closer in, so has a shorter distance to propagate - and hence a shorter lag time - before it modulates the spectrally hardest inner regions (Mahmoud & Done 2017, hereafter MD17). If instead the hot flow were homogeneous, spectra from the outer and inner radii would be the same, so low and high-energy lightcurves would sample emission from the same radii in the same proportions, resulting in no lag between them.

Thus the observed lag between different energy bands which are both dominated by Comptonisation suggests that the spectral and variability properties of the hot flow are radially stratified. The observed spectral variability can therefore in principle be used to determine the radial stratification of the hot flow. This goal is complementary to that of the recent work of Mastroserio, Ingram & van der Klis (2018), where they focus on using the continuum variability to probe the thin disc structure via reverberation, rather than exploring the structure of the continuum source itself.

We develop techniques to use the observed spectral-timing information to build a model of the radial stratification in variability, emissivity and energy spectra, developing significantly from our previous work in MD17. We use this on some of the best available data, that of the Rossi X-ray Timing Explorer (RXTE) observations of Cyg X-1, taken before the telemetry limitations which accompanied the antenna failure. Cygnus X-1 is an ideal source for this study, since there is no obvious QPO to complicate the underlying propagation models. We show simultaneous fits to the time averaged spectra, the frequency resolved spectra, the power spectral densities (PSDs) over different energy bands and the lags between energy bands. We show that we can build a self-consistent picture of all these data with a flow composed of two spectral regions, with the transition from soft to hard spectra at very small radii (within $2-5 R_g$ of the black hole) associated with a large peak in both the variability and the emissivity. Alternatively, a three component spectral model gives less extreme, larger radii with maximal variability and emissivity generated in an intermediate region from $8-9 R_g$. While we cannot break all the degeneracies, we show that the data fundamentally require spectrally distinct regions within

the Comptonisation zone, and that the variability and emissivity are jointly enhanced at specific radii. This is especially marked for the softest spectral component, where the data also point to a break in variability timescale between this and the rest of the hot flow. In this picture, the flow consists of a number of bright, turbulent rings rather than being a smooth, self-similar structure. This picture is very different to the original assumption that variability is dominated by the self-similar turbulence of the Magneto-Rotational Instability (MRI), which remains the physical mechanism behind the angular momentum transport in the flow (e.g. Noble & Krolik 2009, as used by Ingram & Done 2011, hereafter ID11; Ingram & Done 2012a). The bright, turbulent radii we identify must be important in understanding the physics of the flow, and we suggest identifying these with the disc truncation radius, the ‘bending wave’ or nonaxisymmetric tilt-shock radii seen in Magnetohydrodynamic simulations (MHD; Lubow, Ogilvie & Pringle 2002; Fragile et al. 2007; Generozov et al. 2014), and/or the jet launch radius.

In the following we denote radii as $r = R/R_g$, where $R_g = GM_{BH}/c^2$.

2 ANALYTIC MODELLING

In MD17 we carried out all simulations of the mass accretion variability in the hot flow using a numerical procedure adapted from the method of AU06 and ID11. In that method, the mass accretion rate curve in each annulus, r_n , was generated by sampling from a zero-centered Lorentzian with a cut off at the local viscous frequency, $f_{visc}(r)$,

$$|\tilde{m}(r_n, f)|^2 \propto \frac{F_{var}(r_n)^2}{1 + [f/f_{visc}(r_n)]^2} \left[\frac{\sin(\pi f dt)}{\pi f dt} \right]^2, \quad (1)$$

and transforming to the time domain via the Timmer and König (1995; hereafter TK95) algorithm. dt here denotes the time resolution of the simulations, and $F_{var}(r_n)$ is the fractional variability per radial decade at r_n . These mass accretion rate curves were then lagged and multiplied together to simulate propagation through the flow, and the final time series were weight-summed to produce the light curves in each band.

However these simulations are slow. The basis for a fast procedure to produce the energy-dependent PSDs was also adapted in MD17 from the groundbreaking analytic formalism of Ingram & van der Klis 2013, hereafter IvdK13. This analytical method can produce results consistent with those of the TK95 algorithm when spectral constraints are also included. In this work we will use this faster technique to enable us to search through the wide parameter space generated by the multiple components of the model. The updated formalism is described in rigorous detail in Appendix A, but we give an overview of the physical parameters below.

2.1 Spectral Stratification

Fundamentally, the model assumes a changing spectral shape as a function of radius, $F(E, r)$. In the simplest case, it describes a hot flow stratified into two regions, each of which produce a different spectral shape. A Soft spectral component, $S(E)$, is produced in the outer region, while the inner region produces a Hard spectral component $H(E)$. $S(E)$,

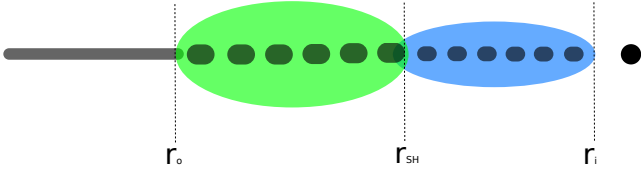


Figure 1. The physical geometry of the flow assumed in the two Compton component model. The dark grey region denotes the thermal, thin disc which does not vary on fast timescales. The green region denotes the fast-varying, spectrally Soft zone, the cyan region denotes the fast-varying, spectrally Hard zone. Mass accretes down the flow from the disk truncation radius at r_o , through the Soft-Hard transition radius at r_{SH} , toward the inner flow radius at r_i . The black ellipses in the flow denote thermal clumps torn from the disc at the truncation radius which provide seed photons for local Comptonisation. These clumps shrink as they pass through r_{SH} due to (any of) the MRI response, frictional stripping, and/or processes at the spectral switch radius.

$H(E)$ and their reflected components are determined from direct fitting of a two Compton component model to the total spectrum, further details of which are described in Section 4. For Soft and Hard Comptonisation components (and their reflections) $S(E)$, $H(E)$, $R_S(E)$ and $R_H(E)$, the time-averaged spectrum associated with each radius is given by

$$\bar{F}(E, r_n) = \begin{cases} S(E) + R_S(E) & \text{if } r_n > r_{SH}, \\ H(E) + R_H(E) & \text{if } r_n < r_{SH}. \end{cases} \quad (2)$$

r_{SH} here is the transition radius between the Soft and Hard Comptonisation regions. This is analytically derived from the radial scale, the spectral components $S(E)$ and $H(E)$, and the prescribed emissivity (parameterised in Section 2.3) such that the luminosity ratio between the two direct components matches that of the emissivity, via

$$f_H^S = \frac{\int_E S(E) dE}{\int_E H(E) dE} = \frac{\int_{r_o}^{r_{SH}} \epsilon(r) 2\pi r dr}{\int_{r_{SH}}^{r_i} \epsilon(r) 2\pi r dr}. \quad (3)$$

To calculate light curves in different energy bands from our simulation, we weight the mass accretion rate at each annulus r_n by the product of the emissivity at r_n , and the integrated spectral components of equation (2), folded with the detector response and interstellar absorption (see equation A8). Including the detector response and interstellar absorption ensures that the simulated data is weighted in the same way as the observations.

Regarding equation (2), we note two assumptions of our model. First, we do not consider the light travel delay between the continuum and reflected emission. Given a typical light travel time of 1 ms implied by a typical disc truncation radius of $15 R_g$ (of order \sim our final fit values of Table 5), the reflection lag should be negligible at low frequencies where the Hard lag is of order 100 ms. However in reality, continuum emission may be reflected from much further out on the disc, as described by a more physical transfer function (see e.g. Gilfanov, Churazov & Revnivtsev 2000). This would result in a more significant reflection lag contribution.

We also assume no spectral pivoting in our case, i.e. that the observed variability relates only to variation in the normalisation of each spectral component, not from a changing shape. Other models have investigated spectral pivoting in modelling the timing of BHBs (e.g. Veledina 2016) and Ac-

tive Galactic Nuclei (Gardner & Done 2014). Most recently, Mastroserio, Ingram & van der Klis (2018) used spectral pivoting to fit to the complex covariance of this Cyg X-1 data, in order to phenomenologically model the continuum lags and constrain the reverberation lags from the disc. We note however that the unphysically small inner radius of $1.5 R_g$ they derive could be due in part to their assumption that the continuum lags arise from pivoting rather than our assumed different spectral components. We will explore the assumptions regarding both reflection and spectral pivoting in more detail in a future paper.

Once $S(E)$, $H(E)$, $R_S(E)$ and $R_H(E)$ are established from the spectrum, the model then solves for parameters which set the radial dependencies of the flow, including

- (i) The radial propagation speed $v_r(r) = r f_{visc}(r)$
- (ii) The fractional variability per radial decade, $F_{var}(r)$
- (iii) The total emissivity, $\epsilon(r)$
- (iv) Propagation losses of variability amplitude. This occurs due to either smoothing by the Green's function response of the flow, and/or damping due to macroscopic turbulent processes.

We specify these parameters in detail below, using previous results as the basis to set the minimum number of free parameters required to reproduce the features seen in these data.

2.2 Propagation Speed

In simple propagating fluctuations models, the viscous frequency often follows $f_{visc}(r) = B r^{-m} f_{kep}(r)$ where $f_{kep}(r)$ is the Keplerian frequency. This sets the frequency at which fluctuations are generated at r via equation (1). Here we assume that this also sets the propagation speed, $v_r(r)$, through $v_r(r) = r f_{visc}(r)$. As we show in Appendix B, the viscous timescale therefore determines not only the peak positions in the PSD, but also the time lag between energy bands.

In MD17, we used the association of the low frequency QPO with Lense-Thirring precession (see Ingram et al. 2016) to set $B = 0.03$ and $m = 0.5$. This was required to reproduce the relation between the low frequency power spectral break and the QPO frequency ($f_{lb} - f_{QPO}$; ID11). This relation correlates the low-frequency noise near f_{lb} - that generated in the outermost regions of the flow - with the QPO frequency assuming solid-body precession of the entire hot flow.

However the low frequency break could instead be set by fluctuations from the inner edge of the disc rather than fluctuations in the hot flow itself. In this work, we therefore assume that $B = 0.03$ and $m = 0.5$ in the outer part of the flow, but we also explore whether the inner flow has a distinct propagation speed, as might be expected from the transition between the thin disc and the hot flow (Hogg & Reynolds 2017). Where the spectral shape switches from Soft to Hard, the physical process resulting in the different spectrum may also be associated with a different viscosity form. We therefore parameterise the viscous timescale as

$$f_{visc} = \begin{cases} B_S r^{-m_S} f_{kep}(r) & \text{if } r \geq r_{SH} \\ B_H r^{-m_H} f_{kep}(r) & \text{if } r < r_{SH}, \end{cases} \quad (4)$$

where B_S , m_S , B_H and m_H are model parameters for the viscosity in the Soft and Hard regions. Regardless of the internal variability processes of the flow at $r \ll r_o$, the $f_{lb} - f_{QPO}$

relation should hold, so we fix $B_S = 0.03$ and $m_S = 0.5$. However we do allow B_H and m_H to vary, as the inner-region viscosity is not constrained by the QPO.

We note that some previous works (e.g. Ingram & Done 2012a, Rapisarda et al. 2016, Rapisarda, Ingram & van der Klis 2017a, hereafter R17a) have instead used a viscous frequency profile for the flow which smoothly varies with surface density, this form being inferred from MHD simulations. However those works also assume smooth, MRI-driven turbulence and emission profiles, as these were satisfactory to explain their data given the lack of spectral constraints. In the new picture we are exploring - of quasi-limited regions enhancing the variability, and in particular of the thin disc being shredded in the Soft region - it becomes inconsistent to think of the viscous timescale as being a smooth function of radius. This motivates the broken profile of equation (4).

2.3 Correlated Turbulence and Emissivity in a 2-Component Flow

MD17 principally showed that the ‘bumpy’ power spectra seen in the low/hard state of Cyg X-1 and other sources (Churazov, Gilfanov & Revnivtsev 2001; Pottschmidt et al. 2003; Axelsson et al. 2008; Torii et al. 2011; Misra et al. 2017; GX 339-4: Nowak 2000) cannot be matched by self-similar turbulence where $F_{var}(r)$ is constant. Regions of enhanced variability over a very small range in radii are required in order to produce an excess of power over a limited frequency range. These may be physically associated with the transition from the thin disc to the hot flow, nonaxisymmetric shocks at the inner radius of the flow if this is tilted with respect to the black hole spin (Henisey, Blaes & Fragile 2012; Genereozov et al. 2014) or the jet/flow interaction.

The PSDs at all energies in our data show three distinct bumps (e.g. the shaded regions in Fig. 4(a)), so we parameterise $F_{var}(r)$ phenomenologically as a sum of three gaussians, with width, σ_{en}^i , radial position, r_{en}^i and amplitude, A_{en}^i , giving

$$F_{var}(r) = \sum_{i=1}^3 A_{en}^i e^{-\frac{r-r_{en}^i}{2\sigma_{en}^i}}. \quad (5)$$

One very natural source of this variability is at the truncation radius, where the interaction between the between the Keplerian disc and sub-Keplerian flow is likely to be highly unstable. We therefore associate the outermost gaussian in $F_{var}(r)$ with the truncation radius so that $r_{en}^1 = r_o$. Incorporating equation (5) into the model allows it the freedom to significantly vary the amount of turbulence within the flow as a function of position. The physical pictures which can be inferred from the fits can therefore range from the traditional propagating fluctuations model (broad, low amplitude Lorentzians would give roughly constant fractional variability produced at all radii, driven the MRI), to the case of certain processes dominating the variability at distinct radii, potentially independent of MRI turbulence.

We force positive-definite resulting lightcurves by setting a prior limit to $F_{var}(r)$ such that the rms variability generated in any region has $0 < \sigma(r) < 0.5$ ($\sigma(r) = F_{var}(r)/\sqrt{N_{dec}}$ where N_{dec} is the number of annuli per radial decade). Models which go above this limit are simply flagged as infinitely bad in terms of goodness of fit (see Section 3).

However, to make an impact on the power spectra, regions of enhanced variability should form a significant contribution to the resulting lightcurves. This requires that they modulate a large fraction of the total luminosity. It is difficult to do this with a smooth emissivity (as assumed in MD17) as this limits the contribution to the lightcurve from any small range of radii. The impact of the region in the lightcurve is the product of the variability power and the integrated emissivity over the radial range at which the excess turbulence is produced. With the smooth emissivity assumption, the additional variability required to fit the data is so large that the assumption of linearity in the generated lightcurves is broken (MD17). This results in the lightcurves becoming negative, which is unphysical!

We now link the turbulence to the emissivity of the flow, such that the more variable regions produce a larger proportion of the emission. This is motivated not only by the demands of the data, but also by the findings of MHD simulations which show that turbulence is inherently dissipative (see e.g. Blaes 2013). We parameterise the enhanced emissivity regions with three Gaussians, tied to the same radii and width as for the turbulence above, but with free normalisation. We also assume that this occurs on the background of a smooth $\epsilon(r)$ with index γ in order to encode the joint contributions from the turbulence and gravitational energy release to the energetic dissipation. We then have

$$\epsilon(r) \propto r^{-\gamma} \left(e^{-\frac{r-r_{en}^1}{2\sigma_{en}^1}} + Z_\epsilon^2 e^{-\frac{r-r_{en}^2}{2\sigma_{en}^2}} + Z_\epsilon^3 e^{-\frac{r-r_{en}^3}{2\sigma_{en}^3}} \right), \quad (6)$$

where Z_ϵ^2 and Z_ϵ^3 are the relative amplitudes of the second and third Gaussians to that of the first.

In Fig. 2(a) & (b) we show the schematic for the revised $F_{var}(r)$ and $\epsilon(r)$ profiles with arbitrary normalisation on both, illustrating how these profiles are now associated in terms of the positions and radial scales of the enhanced regions.

2.4 Smoothing and Damping

Another key feature often seen in the Cyg X-1 low/hard state which previous models have been unable to replicate is the suppression of low-frequency correlated variability associated with lower energy bands compared to higher energy bands (e.g. Grinberg et al. 2014, Rapisarda, Ingram & van der Klis 2017b; MD17). This feature is also seen in other BHBs including SWIFT J1753.5-0127 and GX 339-4 (Wilkinson & Uttley 2009), and so is likely generic to the low/hard state paradigm. For similar Low and High energy power spectral shapes (i.e. no preferential suppression of certain frequencies between bands), the timing properties can be jointly fit using simple propagating fluctuations, but when the power spectral shapes become distinct at low frequencies, the lags in each band become dominated by different spectral components and joint fits fail (Rapisarda, Ingram & van der Klis 2017a). This implies that the variability present in the spectrally softer regions is not completely propagated down to modulate the harder regions. Yet the fact that there are lags between Low and High bands on the timescale of the outer parts of the flow means that at least *some* of the variability does propagate. The variations in the Soft region must therefore map onto the inner-region variability after propagation, although with smaller amplitude and a time delay.

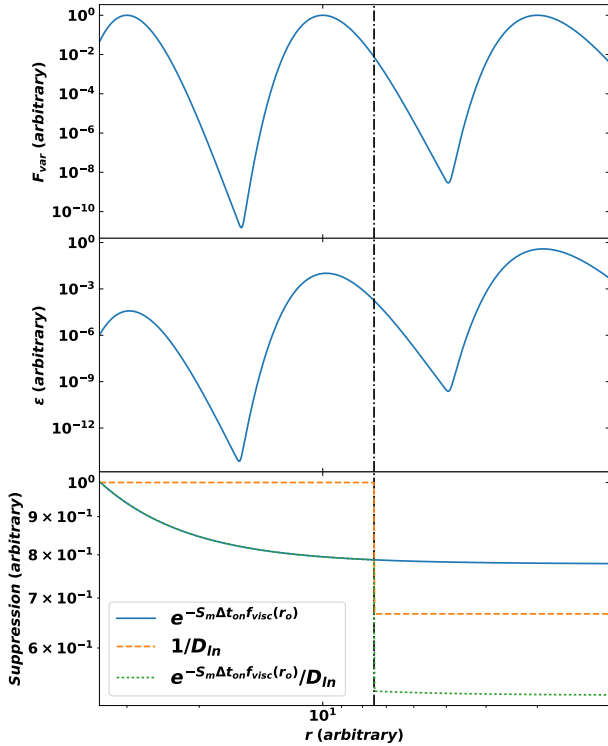


Figure 2. Top panel (a): generic schematic of the fractional variability profile used in the model. Middle panel (b): generic schematic of the emissivity profile used in the model (blue solid line), with a Novikov-Thorne-type $\epsilon(r) \propto r^{-3} (1 - \sqrt{r_i/r})$ profile for comparison. Comparing panels (a) and (b), we illustrate that the location of the humps in variability correspond to those in the emissivity, from the assumption that turbulence ties to energetic dissipation. Bottom panel (c): generic schematic of the smoothing/damping profiles, denoting the effect of damping (orange, dashed line), an example of smoothing (blue, solid line), and the product of these as used in the model (green, dotted line). Note that we only show an *example* of smoothing at a single frequency propagating from the truncation radius (that of $f_{visc}(r_o)$), while smoothing is actually a two-dimensional function of frequency and propagation time. The black dot-dashed line denotes the spectral transition radius, r_{SH} .

Our model includes two distinct methods of variability suppression. First, there can be diffusion of fluctuations as they propagate through the flow due to the Green’s function response (e.g. R17a). This acts to preferentially smooth out the fluctuations which have propagated over a larger distance compared to their wavelength. We follow R17a and model this as an exponential decay such that all fluctuations of frequency f which propagate from r_i to r_n (which takes timescale Δt_{ln}) are suppressed by a continuous factor $\exp(-S_m \Delta t_{ln} f)$. Here

$$\Delta t_{ln} = \sum_{k=1}^{n-1} dt_k = \sum_{k=1}^{n-1} \frac{dr_k}{r_k} t_{visc}(r_k) = d \log(r) \sum_{k=1}^{n-1} t_{visc}(r_k). \quad (7)$$

However, our model fundamentally includes regions of enhanced variability/emissivity. The specific processes which generate this additional power could also suppress the propagating fluctuations at the associated radii. In our

nomenclature, we will refer to the process of suppressing power at all frequencies uniformly at specific radii as ‘damping’, distinct from the diffusive smoothing process discussed above, which instead has a frequency/travel time dependence. We tie our damping effect to the radius at which the spectral shape changes from Soft to Hard, as physically this requires a change in seed photon availability, and these seed photons in the Soft region could be from clumps torn from the inner edge of the truncated disc by the truncation process. These clumps would produce copious, highly variable, seed photons for the Soft region of the flow, making the characteristic Soft, highly variable spectrum (see also Uttley et al. 2011; Grinberg et al. 2014). If they are dissipated upon entering the Hard region, this would result in the hardening of the spectral shape as observed. We therefore suppress all the propagated variability by a single factor D_{SH} at the spectral transition radius, r_{SH} . The grey ‘blobs’ in the flow in Fig. 1 represent these clumps shrinking as they accrete, but we also do not preclude other processes (such as high magnetic flux density near r_{SH}) from being an alternative source of damping, as would be the case if the transition radius is coupled to the jet.

In Fig. 2(c) we show an example of these smoothing and damping effects separately, and in combination. Note that the smoothing in this figure is an example for a fixed frequency, $f = f_{visc}(r_o)$, and in truth smoothing acts as a function of frequency.

3 TIMING FIT PROCEDURE

Producing a fully generalised model which fits the spectra and timing properties simultaneously would be both technically complex and computationally prohibitive. Furthermore, in a parameter space with dimensions corresponding to the free parameters for both the spectral and timing fits¹, degeneracy and correlation between parameters would be a significant concern. With this in mind, we fit first to the energy spectra, and then to the energy-dependent timing properties, to demonstrate the possible achievements and limitations of the model. Unlike the slower TK95 method used in MD17, the fast analytic prescription we use allows us to obtain parameter space minima using the Markov Chain Monte Carlo (MCMC) method via the PYTHON package, EMCEE (Foreman-Mackey et al. 2013). This allows a much more thorough exploration of the parameter space than in MD17, systematically testing the limits of each model. In all analytic model fits, we assume that Cyg X-1 has a black hole of mass $M_{BH} = 15M_\odot$, and a dimensionless spin parameter of $a^* \sim 0.85$ when calculating $f_{kep}(r)$ (Tomsick et al. 2014; Kawano et al. 2017). All spectral-timing fits use $N_r = 70$ logarithmically spaced radial bins, which is a compromise between computational cost and spatial resolution.

To find the timing properties of the data, we extract lightcurves using SAEXTRACT in three energy bands: Low (3.13–4.98 keV), Mid (9.94–20.09 keV) and High (20.09–34.61 keV). These lightcurves are found by co-addition of

¹ In the case of § 5 where three spectral components are used, these are 19 and 18 free parameters respectively.

three consecutive observations of Cyg X-1 (ObsIDs: 10238-01-08-00, 10238-01-07-000, 10238-01-07-00, hereafter Obs. 1-3), where the similar spectra and hardness ratios of these observations justify their co-addition (see MD17). Obs. 1-3 all have 15.6 ms time resolution with 64 energy bins across the entire RXTE PCA energy bandpass (standard channels 0-249; B_16ms_64M_0_249 configuration) giving good spectral resolution in the 3-10 keV band near the FeK α line. We calculate the noise-subtracted power spectra and time lags of the data by ensemble averaging over 174 intervals, each containing 2^{13} time bins of 2^{-6} s length. The power spectra and time lags are then rebinned geometrically such that the number of points in bin J adheres to $N_p(J) \leq 1.11^J$ (van der Klis 1989), with at least a single point in each frequency bin. This produces fully binned power spectra in each band, $P_i(f)$, and lags between bands, $\tau_{ij}(f)$, where $i, j = 1 \dots N$ and N is the number of distinct energy bands. These statistics have corresponding errors $\Delta P_i(f)$, $\Delta \tau_{ij}(f)$. Since each measured frequency is first ensemble averaged over 174 separate intervals, this far exceeds the prerequisite number of points required for the errors to converge to Gaussian at all frequencies (Papadakis & Lawrence 1993), and so chi-squared fitting is appropriate for this data.

To simultaneously fit to the power spectra and time lags, we reduce the sum of the chi-squared values for the power spectra in the Low, Mid and High bands, and a weighted form of the High-Low band time lags; in particular we weight the lags by a factor of three against the power spectra, to ensure an equal balance in fit preference between these statistics. This is preferable to including the unweighted sums of the High-Low, High-Mid and Mid-Low band time lags, since the latter two exhibit large error bars consistent with zero. This would result in an overweighting of the fit statistic toward the power spectra at the expense of the important cross-spectral lag information. The statistic we reduce is therefore

$$\chi^2 = \sum_{j=1}^J \left\{ \frac{[P_{Lo}^{mod}(f_j) - P_{Lo}^{obs}(f_j)]^2}{\Delta P_{Lo}^{obs}(f_j)^2} + \frac{[P_{Mid}^{mod}(f_j) - P_{Mid}^{obs}(f_j)]^2}{\Delta P_{Mid}^{obs}(f_j)^2} + \frac{[P_{Hi}^{mod}(f_j) - P_{Hi}^{obs}(f_j)]^2}{\Delta P_{Hi}^{obs}(f_j)^2} + 3 \frac{[\tau_{LH}^{mod}(f_j) - \tau_{LH}^{obs}(f_j)]^2}{\Delta \tau_{LH}^{obs}(f_j)^2} \right\},$$

where the superscripts *mod* and *obs* refer to the model and observational statistics respectively, and subscripts *Lo*, *Mid* and *Hi* refer to the Low, Mid and High energy bands respectively.

4 SPECTRAL FITS: TWO COMPTON COMPONENTS

In MD17 we fitted the time averaged SED from the 1996 outburst of Cygnus X-1 (Obs. 1), in XSPEC (version 12.9.1; Arnaud, Borkowski & Harrington 1996). The model consisted of two Comptonisation components described by `tbabs * (nthcomp + nthcomp)` (Zdziarski, Johnson & Magdziarz 1996), and their combined reflection, `tbabs * (kdblur * xilconv * twocomp)`, where `twocomp` is a local model which adds the Comptonisation components together. This fit was motivated by model simplicity, and by similar successful fits to Cyg X-1 spectra (Gierliński et al. 1997; Di Salvo et al. 2001; Makishima et al. 2008; Basak et al. 2017). For the

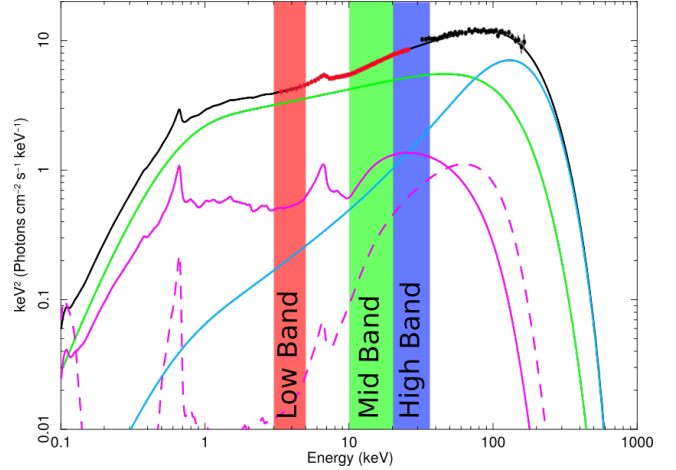


Figure 3. Two component spectral decomposition of Obs. 1 (ObsID: 10238-01-08-00) updated from MD17, denoted model spectral model **A**. Lines show the total energy spectrum (black solid), the Hard Compton component ($H(E)$, cyan solid), the Soft Compton component ($S(E)$, green solid), the truncated disc reflection from the Hard component ($R_H(E)$, magenta dashed), and the reflection from the Soft component ($R_S(E)$, magenta solid). Filled circles show the PCA (red) and HEXTE (black) data. The red, green and blue bands denote the Low (3.13-4.98 keV), Mid (9.94-20.09 keV) and High (20.09-34.61 keV) energy ranges respectively.

first spectral fit of this paper, we use a slightly revised version of the MD17 model, `tbnew_gas * (nthcomp + nthcomp + kdblur * xilconv * (nthcomp + nthcomp))`², where we now separate the reflected components to be consistent with the revised formalism of equation (2). We use 1% systematic errors in the PCA bandpass in this fit³. As in MD17 we have followed Makishima et al. (2008) who fix the seed photon temperature for both Compton components to that of the disc at 0.2 keV, and tie the electron temperatures of both components. This remains the best possible fit to this data given these constraints, although the reduced chi-squared is poor ($\chi^2_\nu = 254.6/91$); in Section 4.2 we will look at how releasing these constraints can in fact lead to a better fit to the total and Fourier-resolved spectra. In Fig. 3 we show the broadband spectral fit which exhibits very similar behaviour to MD17, as required. The dominant Soft (green) and Hard (cyan) Compton components are produced from the outer and inner regions of the flow respectively. Also included is the reflection from the Soft component (magenta solid), and from the Hard component (magenta dashed), but we do not include the intrinsic or reprocessed disc emission as the energy of this is too low to make a significant contribution to the RXTE data above 3 keV. We denote this as spectral model **A**, with full parameters detailed in Table 1.

Fig. 4 shows the optimal joint fit to the PSDs of all three energy bands and to the High-Low band time lags ob-

² `tbnew_gas` is the new, faster version of `tbabs` (Wilms, Allen & McCray 2000), and can be found here:

<http://pulsar.sternwarte.uni-erlangen.de/wilms/research/tbabs/>.

³ This systematic error is used for consistency with later fits in this paper which incorporate Fourier-resolved spectra, using 1% PCA systematics as in Axelsson & Done (2018).

Spectrum	Γ_S	$kT_{e,S}^{\dagger}$ (keV)	n_S	Γ_H	$kT_{e,H}^{\dagger}$ (keV)	n_H	$(\frac{\Omega}{2\pi})_S = (\frac{\Omega}{2\pi})_H$	$\log(x_i)$	χ^2/dof
Total	$1.784^{+0.003}_{-0.001}$	$39.2^{+0.9}_{-0.3}$	$2.187^{+0.001}_{-0.009}$	$1.25^{+0.010}_{-0.002}$	$39.2^{+0.9}_{-0.3}$	$0.065^{+0.001}_{-0.002}$	$-0.252^{+0.001}_{-0.002}$	$3.000^{+0.004}_{-0.001}$	254.6/91

[†]These are tied.

Table 1. Fitting parameters for spectral model **A**, described by `tbnew_gas * (nthcomp + nthcomp + kdblur * xilconv * (nthcomp + nthcomp))`. This shows fit parameters close to that of MD17, only now with separate reflection from each Compton component. n_m and $(\frac{\Omega}{2\pi})_m$ denote the normalisation and reflection fractions on Compton component m . Uncertainties are quoted at the 1σ confidence level. The associated spectrum is shown in Fig. 3.

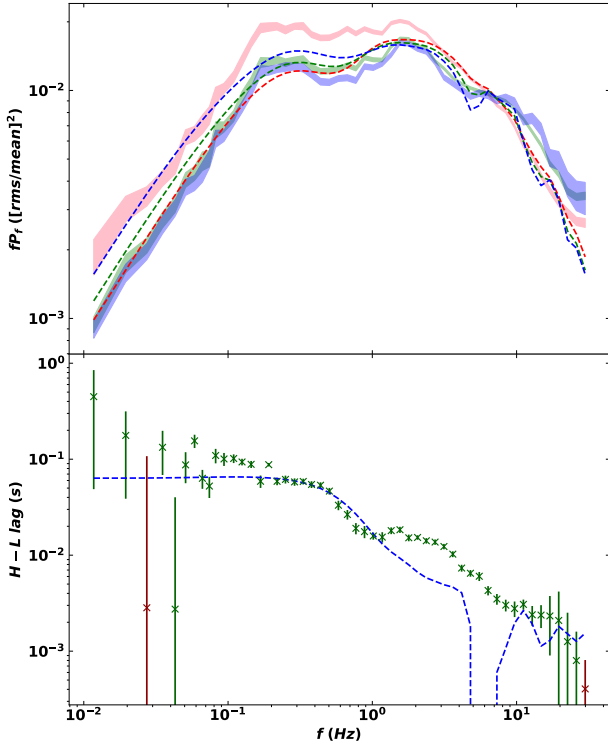


Figure 4. Timing fit using spectral model **A**. Top panel (a): High, Mid & Low band PSDs. The shaded regions are the 1σ error regions of the Low (pink), Mid (green) and High (blue) energy bands from the data. The solid lines show the Low (red), Mid (green) and High (blue) energy model outputs. Bottom panel (b): High-Low band time lags for the data (crosses) and models (circles). Green (red) crosses indicate the High band lagging the Low band (or vice versa). Black (purple) circles indicate the High band lagging the Low band (or vice versa).

tained using spectral model **A**. The parameters of this fit are presented in Table 5, along with parameters for all other spectrally-constrained timing fits shown in this paper. The model can fit well to the low-frequency lag, and qualitatively replicates the humped structure of the power spectra. The reason for the good match to the low-frequency lag is clear from the $F_{var}(r)$ and emissivity profiles of Fig. 5(a) & (b). Significant variability is present in the outer parts of the flow, and the emissivity hump near r_o means that more emission is produced from these outer annuli. This results in a larger ‘characteristic’ propagation time from the Soft to

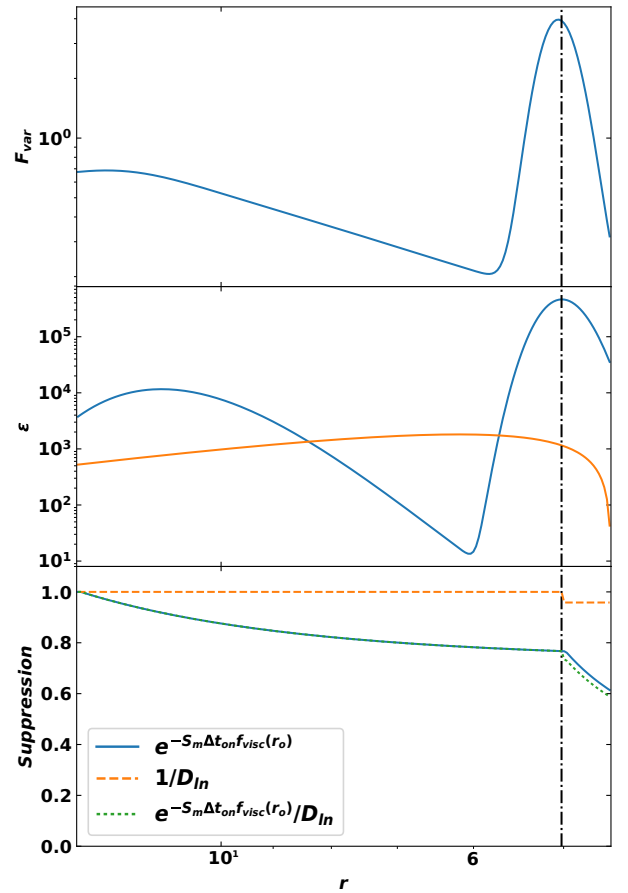


Figure 5. Fractional variability (F_{var} , top panel (a)), emissivity (ϵ , middle panel (b)) and smoothing/damping (bottom panel (c)) profiles found for fit of Fig. 4. Colours and linestyles as in Fig. 2.

Hard region, sufficient for the long lags seen in the data (see equation B1 and Fig. B1).

The fit to these qualitative features are interesting, however they have come at the expense of the high-frequency lags, partly due to over-smoothing shown by the high value of $S_m = 0.61$ (Fig. 5c). This fit also fails in the hierarchy of power spectra below 2 Hz and above 10 Hz, which are opposite to what is seen in the data, probably due to the fit tendency toward under-damping with $D_{SH} = 1.04$. However these incorrect smoothing and damping parameters were likely converged upon due to the fundamental problem of spectral model **A**, which similarly struggled to fit simultane-

Spectral Fit	n/a	B	n/a
PSDs, Lags	Fig. 6	Fig. 9	-
χ_{SH}^{Lo}	0.186	4.21	4.24 [†]
χ_{SH}^{Mid}	0.0803	0.126	0.561
χ_{SH}^{Hi}	0.0424	0.0198	0.243
f_H^S	0.884	0.214	1.32

[†] $\chi_{SH}^{Lo} > 4.2$ constraint imposed here by the findings of spectral fit **B**.

Table 2. Soft : Hard component contributions to the Low, Mid and High bands for the case of values fit directly to the timing properties (Fig. 6), those fixed by spectral fit **B** (Fig. 9), and the final direct fit to the timing with χ_{SH}^{Lo} constrained (figure not shown due to lack of fit improvement).

ously with the lags in MD17. We will therefore now examine what our new timing model can achieve when fitting only to the power spectra and time lags, with no prior fit to the energy spectra.

4.1 Removing the Spectral Priors

Reworking the model to require no prior spectral fit can be done quite simply, by rewriting equation (A8), which describes the weighting of the mass accretion rate curve in each annulus when calculating the light curve in each band. Recasting the energy-dependent part of this equation, we get

$$w_n^{band}(r_n) = \frac{\epsilon(r_n)r_n dr_n}{\sum_{region} \epsilon(r_n)r_n dr_n} \int_{E=E_{band}^{min}}^{E_{band}^{max}} \bar{F}(E, r_n) A_{eff}(E) e^{-N_H(E)\sigma_T} dE$$

$$= \frac{\epsilon(r_n)r_n dr_n}{\sum_{region} \epsilon(r_n)r_n dr_n} L_{comp}^{band}(r_n). \quad (8)$$

Since we are dealing with only two Compton components, $L_{comp}^{band}(r_n)$ here must take one of only six values depending on the energy band and radial zone, so we have

$$L_{comp}^{band}(r_n) = \begin{cases} L_S^{band} & \text{if } r_n > r_{SH}, \\ L_H^{band} & \text{if } r_n < r_{SH}, \end{cases} \quad (9)$$

for each of the three bands. Usefully, the rms normalisation on the power spectra and cross spectra of equations (A13) and (A14) mean that in calculating timing statistics, we actually require only the *ratio* of integrated fluxes from each component in each band, $\chi_{SH}^{band} = L_S^{band}/L_H^{band}$, rather than the L_{comp}^{band} values themselves. We can also remove the necessity for a spectral prior in determining r_{SH} by simply allowing f_H^S (in equation 3) to be free⁴. This leaves us with four additional free parameters in the absence of a prior spectral fit: f_S^H , χ_{SH}^{Lo} , χ_{SH}^{Mid} , χ_{SH}^{Hi} .

⁴ Since f_H^S is highly degenerate with the emissivity, we do not draw any inferences from its fit value.

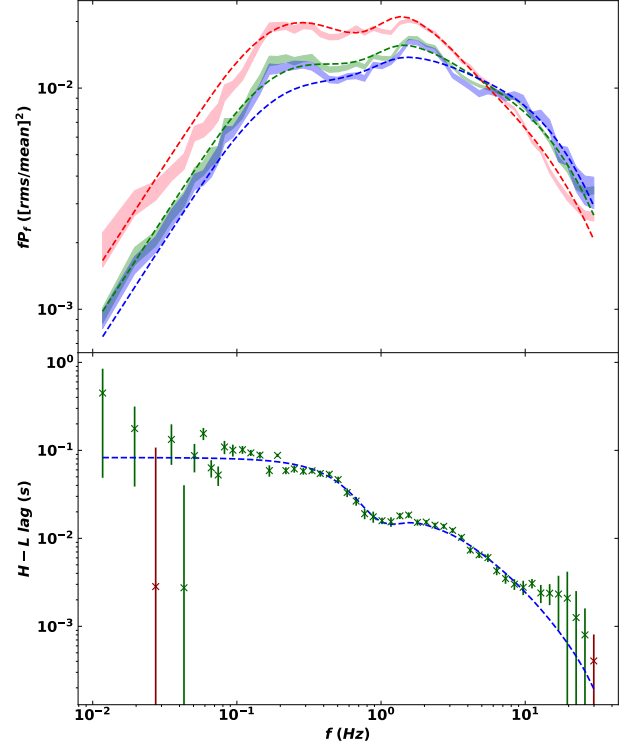


Figure 6. Timing fit with free spectral weights on all components, using the formalism of equations (8) and (9). Top panel (a): High, Mid & Low band PSDs. Colours as in Fig. 4(a). Bottom panel (b): High-Low band time lags. Colours and symbols as in Fig. 4(b).

The best fit for this model, shown in Fig. 6, shows remarkable agreement with the data in both the power spectral and timing behaviour, with the PSD hierarchies and structure, and timing structure, well reproduced. However on examining the final fit values of χ_{SH}^{Lo} , χ_{SH}^{Mid} and χ_{SH}^{Hi} in Table 2, it seems that the spectral picture required by the timing data is that of a Soft Compton component which decays monotonically with energy, providing less than 20% contribution to the flux even in the Low energy band, where we might expect it to dominate. Certain fits (e.g. Di Salvo et al. 2001; Basak et al. 2017) have pointed toward such a picture where the Hard component dominates at all energies above ~ 1 keV, with only a minute Soft Compton contribution at low energies. However these fits have lacked a key tool which we can now use to further constrain the spectrum, extracted from the timing data itself. This tool is the Fourier-resolved (phase-resolved) spectrum.

4.2 Constrained by the Fourier Resolved Spectra

To place further constraints on the spectral fit, we now draw on the Fourier-resolved (FR) spectra found using the technique of Axelsson & Done (2018). These spectra are derived from the first, second and third humps in the total power spectrum of Obs. 1 (designated here as the ‘slow’, ‘intermediate’ and ‘fast’ variability respectively). In Fig. 7, the slow,

Spectrum	Γ_S	$kT_{e,S}$ (keV)	n_S	Γ_H	$kT_{e,H}$ (keV)	$kT_{seed,H}$ (keV)	n_H $\times 10^{-2}$	R_{in} (R_g)	$(\frac{\Omega}{2\pi})_S$	$(\frac{\Omega}{2\pi})_H$	$\log(x_i)$	χ^2/dof
Total	1.85 ± 0.03	$1.7^{+0.1}_{-0.1}$	$2.04^{+0.14}_{-0.07}$	1.69 ± 0.01	105^{+13}_{-9}	3.05 ± 0.13	2.3 ± 0.2	13^{+9}_{-4}	-1.1 ± 0.2	-	$3.3^{+0.2}_{-0.3}$	78.9/167
Slow FR	"	"	0.43 ± 0.03	"	"	"	$0.37^{+0.01}_{-0.02}$	"	"	-	"	
Int. FR	"	"	0.43 ± 0.02	"	"	"	$0.41^{+0.03}_{-0.02}$	"	"	-	"	
Fast FR	n/a	n/a	n/a	"	"	"	$0.262^{+0.007}_{-0.009}$	n/a	n/a	n/a	n/a	

Table 3. Fitting parameters for the two component spectral model **B**, described by `tbnew_gas * (nthcomp + nthcomp + kdblur * xilconv * nthcomp)`, fit to the total and FR spectra simultaneously. n_m and $(\frac{\Omega}{2\pi})_m$ denote the normalisation and reflection fractions on Compton component m . Uncertainties are quoted at the 1σ confidence level. Associated spectra are shown in Figs. 7 & 8.

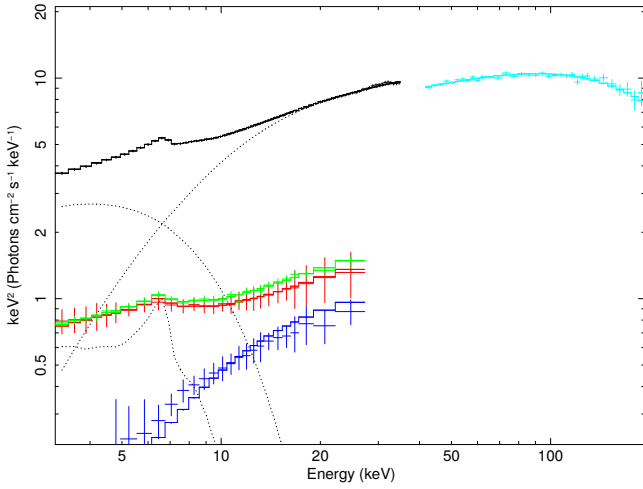


Figure 7. Two component simultaneous fit **B**, fit to the total spectrum from Obs. 1 and the Fourier-resolved components. Shown are the total energy spectrum in the PCA band (black crosses) and fit (black solid line), with fit components (black dashed lines), and the total spectrum in the HEXTE band (cyan crosses) and fit (cyan solid line), with fit components (cyan dashed lines). We also show the FR spectrum for the slow variability (red crosses), and its fit (red solid line), the FR spectrum for the intermediate variability (green crosses), and its fit (green solid line), and the FR spectrum for the fast variability (blue crosses), and its fit (blue line). These FR components are fit using linear combinations of the Soft, Mid and Hard Compton components and their reflection, as detailed in the text.

intermediate and fast FR spectra are shown as the red, green and blue crosses respectively.

The most obvious fact on comparison of the FR spectra is that the fast component is highly distinct from the other two, with a much steeper slope down to its minimum resolved energy. Since this fast variability corresponds to where $f_{visc}(r)$ is highest, it must derive from the innermost, and therefore the hardest, region. The fast FR component therefore provides a strong constraint on the shape of the Hard Compton component, showing that its seed photon temperature, $kT_{seed,H}$, should be much higher than that of the Soft, which draws from the (shredding) disc at $kT_{seed,S} = 0.2$ keV. If the seed photons for the Hard component are coming from a source other than the disc (e.g. the Soft region), then the Hard region cannot have a line of sight to the disc. If the Hard region cannot intercept the photons from the disc,

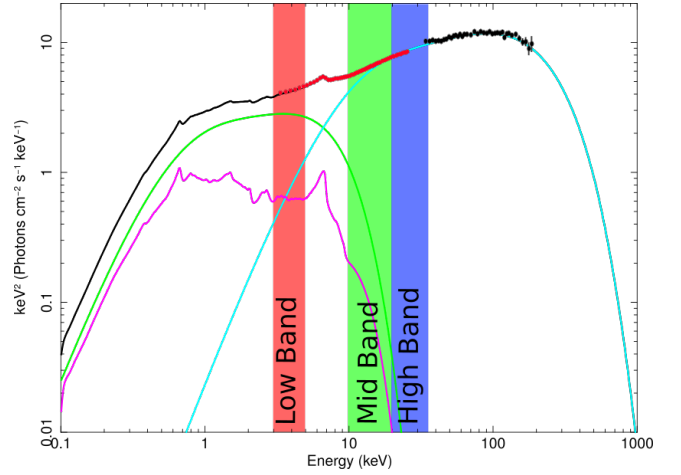


Figure 8. Broadband representation of spectral model **B**. Shown are the total energy spectrum (black), the Hard Compton component ($H(E)$, cyan), the Soft Compton component ($S(E)$, green), and the reflection component ($R(E)$, magenta). Filled circles show the PCA (red) and HEXTE (black) data. The red, green and blue bands denote the Low (3.13-4.98 keV), Mid (9.94-20.09 keV) and High (20.09-34.61 keV) energy ranges respectively.

then the disc in turn must not intercept photons from the Hard region, and so there is no way that the Hard component can produce disc reflection. In the following spectral fits, we therefore switch off reflection from the Hard component [$R_H(E)=0$], in order to keep the spectral model self-consistent.

We now simultaneously fit to the total spectrum from Obs. 1 and its FR spectra, using 1% systematic errors in the PCA bandpass to ensure consistency with Axelsson & Done (2018). Unlike spectral fit **A**, we allow the Hard component seed photon temperature to be free, and untie the Soft and Hard electron temperatures. Since the slow variability is produced in the outer regions, it will propagate through both the Soft and Hard Compton regions. The slow FR spectrum (red crosses with red line fit) is therefore fit with a linear combination of the Soft and Hard `nthcomp` components, along with the reflection from the Soft component. We allow all normalisations of these components to be free, as it is unknown how much of the slow variability propagates into the Hard region. The intermediate FR spectrum (green crosses and solid line in Fig. 7), whose spectral shape is very similar to that of the slow, is similarly fit with a linear

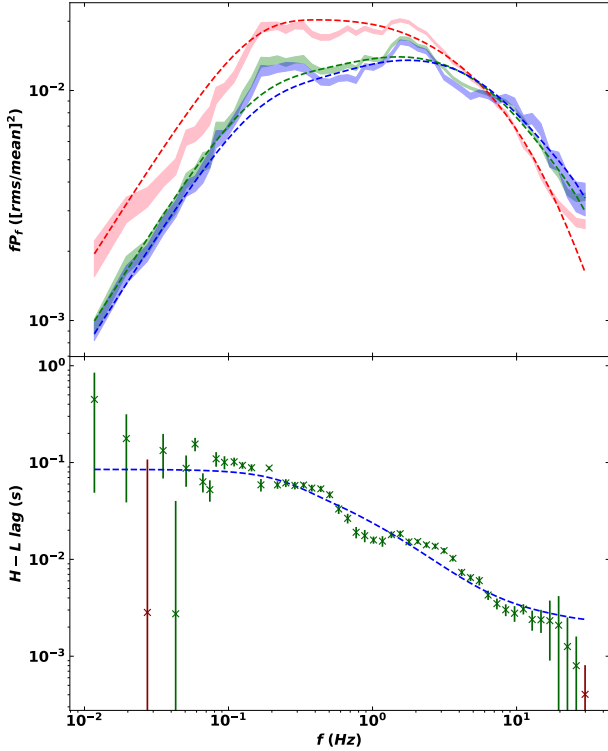


Figure 9. Timing fit using spectral model **B**. Top panel (a): High, Mid & Low band PSDs. Colours as in Fig. 4(a). Bottom panel (b): High-Low band time lags. Colours and symbols as in Fig. 4(b).

combination of the Soft and Hard **nthcomp** components and Soft reflection, again with free normalisations. Finally the fast FR spectrum (blue crosses and solid line in Fig. 7) is fit only with the Hard **nthcomp** component and no reflection, as this variability is produced and seen only in the Hard innermost region, and as mentioned has no direct line-of-sight to the disc. We denote the model fit found here as spectral fit **B**, the parameters for which are shown in Table 3. Despite the additional constraints from the phase-resolved spectra, untying the electron temperatures and the Hard Compton seed photon temperature has produced a dramatic improvement in the fit quality ($\chi^2_v = 59/125$) over spectral fit **A**. We see in the broadband representation of Fig. 8 that we now have a very different spectral picture, where the Soft Compton component is dominant until the iron $K\alpha$ line, switching abruptly to Hard Compton dominance.

When spectral fit **B** is used in the timing model, we arrive at the best fit shown in Fig. 9. The general shape of both the power spectra and the time lags are approximated. The double-broken power law behaviour is achieved with a switch in band dominance at the correct 7 Hz, and the lags decay with the correct slope. However, the finer structure in both cases is not achieved. The smooth hump seen in the PSD is somewhat surprising here, given the commonality between many features of the fit parameters here and in the case of Fig. 4. In both cases, the $F_{var}(r)$ profiles exhibit prominent, separate peaks; in both cases, smoothing is significant, with comparable values of $S_m = 0.61$ and $S_m = 0.46$;

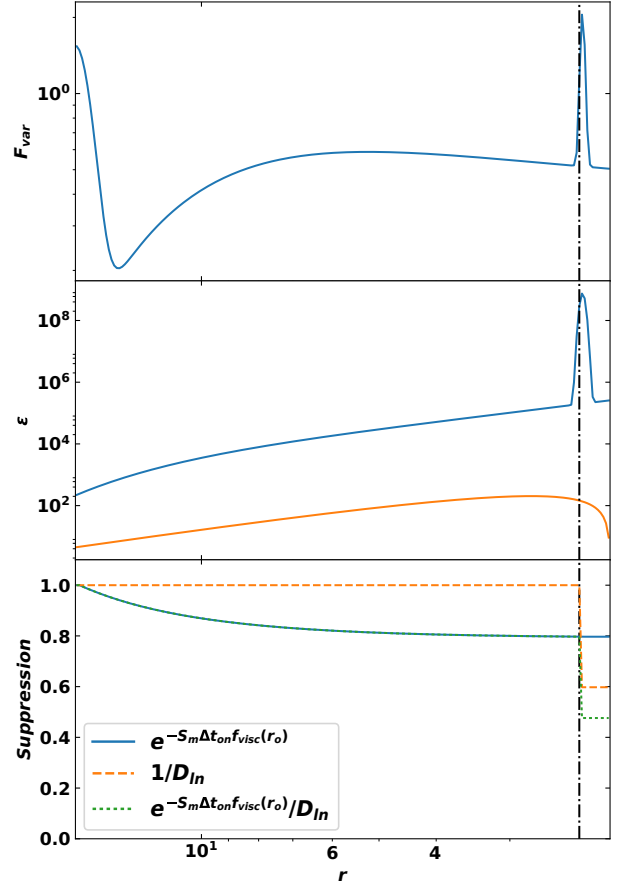


Figure 10. Fractional variability (F_{var} , top panel (a)), emissivity (ϵ , middle panel (b)) and smoothing/damping (bottom panel (c)) profiles found for fit of Fig. 9. Colours and linestyles as in Fig. 2.

in both cases, the viscous timescale in the Hard region is distinct, and in both cases, r_{SH} lies near a peak in the emissivity. Despite this, none of the hump structure is seen here. It cannot therefore be said in full generality that any one of these model features can produce a multi-peaked PSD.

While spectral fit **B** does well to constrain the shape of the Hard Compton component, degeneracy remains between the normalisation of this component and the shape of the Soft component (and its reflection). To truly exhaust our analysis of the two component class of spectral models then, we would like to determine whether there exists *any* spectral fit with two Compton components which satisfies the fast FR spectral shape, fits the energy spectrum, and provides a good fit to the timing properties. To do this, we can use the framework developed in Section 4.1, with one additional constraint.

In spectral fit **B**, the fastest FR component (blue lines and crosses in that figure) was well fit only with the Hard Compton component. The curvature of the Hard component is therefore well constrained until it peaks. In the case of that fit, the Hard component normalisation is maximal, since it contributes all of the photons at energies exceeding ~ 25 keV. This imposes a lower bound on the ratio of Soft to Hard component integrated flux in the Low energy band (χ_{SH}^{Lo})

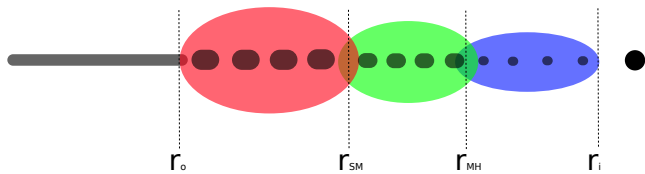


Figure 11. The physical geometry assumed within the flow in the three Compton component model. The dark grey region denotes the thermal, thin disc which does not vary on fast timescales. The red region denotes the fast-varying, spectrally Soft zone; the green region denotes the fast-varying, Mid spectral zone; the blue region denotes the fast-varying, spectrally Hard zone. Mass accretes down the flow from the disk truncation radius at r_o , through the Soft-Mid transition radius at r_{SM} and then the Mid-Hard transition radius at r_{MH} , toward the inner flow radius at r_i . The black ellipses in the flow denote thermal clumps torn from the disc at the truncation radius which provide seed photons for local Comptonisation. These clumps become smaller as they pass through r_{SM} and r_{MH} due to the MRI response, frictional stripping, or both.

of 4.2; for any alternative fit which replicates the fast FR spectrum, the Hard component normalisation may reduce, but it cannot become larger, and its shape cannot change.

We therefore apply the constraint of $\chi_{SH}^{Lo} > 4.2$ to our ‘free spectral weight’ formalism of Section 4.1, to determine whether a better fit exists given only this requirement on the spectrum. This yields a PSD/cross-spectral best fit which shows no improvement in fit quality over Fig. 9 where spectral model *B* was used as a prior; for brevity, we therefore do not show this fit here. From this analysis it appears that no two component model exists which can reproduce the detailed structure in the timing properties simultaneously with satisfying the FR spectra. In particular the lag steps, which are obvious not only in these data, but also in the *Astrosat*/*LAXPC* observations of Misra et al. (2017), are entirely absent when using two Compton components. To find a model which can reproduce the timing features we therefore need to examine more complex spectral decompositions than the two component case, considering a more highly stratified flow than might be suggested by spectral fitting alone.

5 SPECTRAL FIT: THREE COMPTON COMPONENTS

We now consider the effect of decomposing our energy spectrum into not two, but three distinct Comptonisation components, along with reflection from a truncated disc. This is not only motivated from the findings of Section 4, but also from those of other spectral-timing analyses of the low/hard state. In particular, the phase-resolved analysis of Yamada et al. (2013) showed that a highly variable soft spectral component, in addition to the two Compton components initially assumed, was necessary to explain the spectral shape in the 10 – 300 keV band for Cygnus X-1 data ranging from 2005 to 2009.

In our formalism we therefore include an additional Compton component between the Soft and Hard - the ‘Mid’ component, $M(E)$, with reflection $R_M(E)$. In the spectral timing model, the flow is therefore radially stratified into three

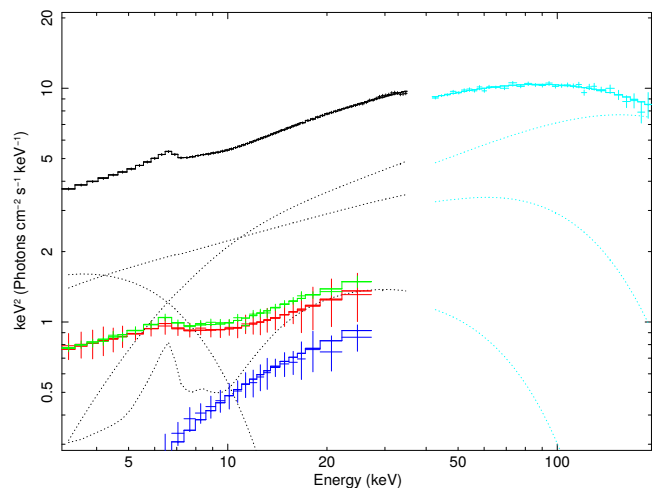


Figure 12. Unfolded three component spectral model *C*, fit to the total spectrum from Obs. 1 and the FR components. Shown are the total energy spectrum in the PCA band (black crosses) and fit (black solid line), with fit components (black dashed lines), and the total spectrum in the HEXTE band (cyan crosses) and fit (cyan solid line), with fit components (cyan dashed lines). We also show the FR spectrum for the slow variability (red crosses), and its fit (red solid line), the FR spectrum for the intermediate variability (green crosses), and its fit (green solid line), and the FR spectrum for the fast variability (blue crosses), and its fit (blue line). These FR components are fit using linear combinations of the Soft, Mid and Hard Compton components and their reflection, as detailed in the text.

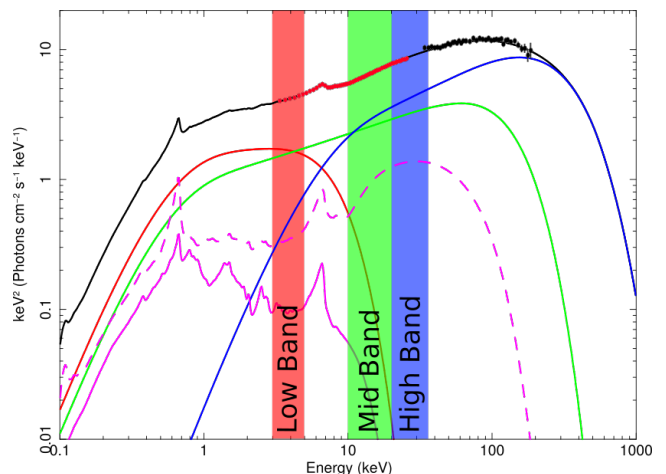


Figure 13. Broadband representation of three component spectral model *C*. Shown are the total energy spectrum (black), the Hard Compton component ($H(E)$, blue), the Mid Compton component ($M(E)$, green), the Soft Compton component ($S(E)$, red), and the reflection component ($R(E)$, magenta). Filled circles show the PCA (red) and HEXTE (black) data. The red, green and blue bands denote the Low (3.13–4.98 keV), Mid (9.94–20.09 keV) and High (20.09–34.61 keV) energy ranges respectively.

Spectrum	Γ_S	$kT_{e,S}$ (keV)	n_S	Γ_M	$kT_{e,M}$ (keV)	n_M	Γ_H	$kT_{e,H}$ (keV)	$kT_{seed,H}$ (keV)	n_H $\times 10^{-2}$	R_{in} (R_g)	$(\frac{\Omega}{2\pi})_S$	$(\frac{\Omega}{2\pi})_M$	$\log(x_i)$	χ^2/dof
Total	1.91	1.67	1.36	1.67	36.1	0.896	1.54	166	2.36	1.75	12.9	-0.539	-0.382	2.90	60.1/158
Slow FR	"	"	0.387	"	"	0.117	"	"	"	0.335	"	"	"	"	
Int. FR	"	"	0.254	"	"	0.224	"	"	"	0.160	"	"	"	"	
Fast FR	n/a	n/a	n/a	n/a	n/a	n/a	"	"	"	0.399	n/a	n/a	n/a	n/a	

Table 4. Fitting parameters for the three component spectral model \mathcal{C} , described by `tbnew_gas * (nthcomp + nthcomp + nthcomp + kdblur * xilconv * (nthcomp + nthcomp))`, fit to the total and FR spectra simultaneously. n_m and $(\frac{\Omega}{2\pi})_m$ denote the normalisation and reflection fractions on Compton component m . Associated spectra are shown in Figs. 12 & 13.

distinct regions with Soft, Mid and Hard spectral shapes, illustrated in Fig. 11. The time-averaged flux from each annulus is therefore

$$\bar{F}(E, r_n) = \begin{cases} S(E) + R_S(E) & \text{if } r_n > r_{SM}, \\ M(E) + R_M(E) & \text{if } r_{MH} < r_n < r_{SM}, \\ H(E) & \text{if } r_n < r_{MH}, \end{cases} \quad (10)$$

where we continue to neglect reflection from the Hard spectral component due to the fast FR spectral shape. Here r_{SM} and r_{MH} are the transition radii between the Soft and Mid, and Mid and Hard Comptonisation regions respectively, analytically derived from the prescribed emissivity such that the luminosity ratios between the Compton components matches that from the emissivity. These radii therefore satisfy the coupled equations

$$\frac{\int_E S(E)dE}{\int_E M(E)dE} = \frac{\int_{r_o}^{r_{SM}} \epsilon(r)2\pi r dr}{\int_{r_{SM}}^{r_i} \epsilon(r)2\pi r dr}, \quad (11)$$

$$\frac{\int_E M(E)dE}{\int_E H(E)dE} = \frac{\int_{r_{SM}}^{r_{MH}} \epsilon(r)2\pi r dr}{\int_{r_{MH}}^{r_i} \epsilon(r)2\pi r dr}.$$

We now fit the time averaged SED, with 1% systematic errors in the PCA bandpass, with three Comptonisation components described by `tbnew_gas * (nthcomp + nthcomp + nthcomp)`, and the reflection of the Soft and Mid components, `tbnew_gas * (kdblur * xilconv * (nthcomp + nthcomp))`. We simultaneously fit this model to both the total and FR spectra. In fitting we assume that the slow variability produced in the outer regions will be seen throughout the flow, and therefore in the Soft, Mid and Hard Compton components. The slow FR spectrum (red crosses and solid line in Fig. 12) is therefore fit with a linear combination of the Soft, Mid and Hard `nthcomp` components, and the Soft and Mid reflection. As in Section 4.2, we allow all normalisations of these components to be free. The intermediate variability (green crosses and solid line in Fig. 12) is also fit with a linear combination of the Soft, Mid and Hard `nthcomp` components with reflection, as an improved fit was found when allowing this spectrum some contribution from all three Compton components. Finally the fast spectral component (blue crosses and solid line in Fig. 12) is satisfactorily fit only with the Hard `nthcomp` component. We show this unfolded fit (denoted spectral model \mathcal{C}) in Fig. 12, with the corresponding broadband shape shown in Fig. 13 and associated parameters shown in Table 4. This fit is somewhat akin to the spectral results of Yamada et

al. (2013), in that we now have a very soft Compton component with a low-energy rollover in $S(E)$, in addition to the other two components, although our Mid component is significantly harder than the one found in their observation.

The introduction of an additional spectral region also requires that the damping parameter of equation (A4) take the form

$$D_{in} = \begin{cases} D_{SM} & \text{if } r_l \leq r_{SM} < r_n < r_{MH}, \\ D_{MH} & \text{if } r_{SM} < r_l < r_{MH} \leq r_n, \\ D_{SM}D_{MH} & \text{if } r_l \leq r_{SM}, r_{MH} \leq r_n, \\ 1 & \text{otherwise,} \end{cases} \quad (12)$$

while the viscous frequency must also be adapted to reflect the use of three spectral regions. This now follows

$$f_{visc} = \begin{cases} B_S r^{-m_S} f_{kep}(r) & \text{if } r \geq r_{SM} \\ B_{MH} r^{-m_{MH}} f_{kep}(r) & \text{if } r < r_{SM}, \end{cases} \quad (13)$$

where B_{MH} and m_{MH} are the viscosity parameters which the Mid and Hard regions share; we do not include distinct timescales for each of these regions for model simplicity.

In our fit to the timing properties using three component model \mathcal{C} , we obtain a best fit shown in Fig. 14. We now find an excellent fit to the lag spectrum up to ~ 10 Hz, exhibiting step features, and even detailed features at 1.5 Hz picked out. The Low energy PSD is also a reasonable match to the data, and although the Mid and High energy band data are lacking some low-frequency power and the first hump, the broadband behaviour is approximated. This fit remains far from perfect, but the qualitative agreement is good. The inferred truncation radius is also consistent with spectral fitting studies at 14.3 R_g (Kolehmainen, Done & Diaz Trigo 2014, $16 \pm 4 R_g$; Basak & Zdziarski 2016, $13 - 20 R_g$). Examining the emission profile in Fig. 15(b), we find an emission profile which is equivalent to two bright “rings” at 8.5 and 5 R_g . The turbulence profile of Fig. 15(a) also exhibits a significant peak at 8.5 R_g , coincident with the Soft-Mid transition radius, indicating a source of extreme variability and emission here, potentially giving rise to the switch in optical depth at this radius. Additional variability is also found at r_o , which would be attributable to disk-flow interaction. The features of variability enhancement at the disc truncation and spectral transition radii (and the emissivity peak at the transition radii), are all shared by the fit of Fig. 9 which used two Compton components, indicating that the data require enhancement of variability at these positions, independent of the true spectral complexity.

The qualitatively good fit we find therefore strongly

suggests that the fundamental model features required to approximate complex spectral-timing data such as these include at least: a non-constant F_{var} profile, a bumpy emission profile corresponding to brighter annuli in the flow, at least three Compton components stratified with radius, and some form of damping of slow fluctuations as they propagate from softer to harder regions. Further complexities may be tested to fit the data in detail, but it would seem that these features are required as a minimum to qualitatively match the lags and PSDs.

With regards to the broken viscous timescale used in fitting, all timing model fits shown in this paper were also run with a smooth viscous profile satisfying the $f_{lb} - f_{QPO}$ relation, i.e. $f_{visc} = 0.03r^{-0.5}f_{kep}(r)$ for all r . Doing so produced only marginally worse fits in all cases (typical $\Delta\chi^2_r \sim 5\%$), although the lag structure in the case of Fig. 14 is qualitatively much better reproduced with a broken viscous timescale. Given that the inclusion of a smooth viscous timescale produces only a minor reduction in fit quality, we therefore do not regard a broken viscous timescale as a fundamental requirement of the model in the same manner as spectral stratification, $\epsilon(r)/F_{var}(r)$ enhancement, and fluctuation suppression.

Here we have shown the effect of using *our* best fits to the total + FR spectra into the timing model. However, even with constraints from the FR spectra, systematic uncertainties on our data mean that the spectral fit itself is subject to degeneracies, and some other three component spectral fit may better represent reality in the accretion flow. Given that the three component model highly over-fits the spectral data alone ($\chi^2_v = 60.1/158$), it is quite likely that a good fit could still be obtained if the timing constraints were incorporated directly into the spectral fit procedure. This would provide a conclusive picture of the accretion geometry. With a view to this, the future aim for this model should of course be the incorporation of XSPEC fitting into the timing fit procedure (or vice-versa), but this remains beyond the scope of this paper.

6 CONCLUSIONS

We expand on the spectral-timing model of MD17 describing the BHB low/hard state, in which fluctuations in the mass accretion rate propagate through a Comptonising, hot flow which is stratified into spectrally distinct regions. We systematically explore the inclusion of more sophisticated profiles for the flow turbulence, emissivity, and spectral shape, and fit these models to some of the best data available for the low/hard state in Cygnus X-1. This data exhibits complex behaviour seen in many low/hard state BHBs, in which low energy bands dominate the power spectra at low frequencies, giving way to high band dominance at high frequencies (e.g. Wilkinson & Uttley 2009; Grinberg et al. 2014). Distinct hard lags, decaying with frequency and featuring ‘steps’ at key frequencies are also seen in this data (Misra et al. 2017), as well as in other sources (e.g. in GX 339-4; De Marco et al. 2015). Such data has not been approximated by a model before (MD17, R17a, Rapisarda, Ingram & van der Klis 2017b). We fit only to data above 3 keV, so that the emission is dominated by the flow, and not by intrinsic disc

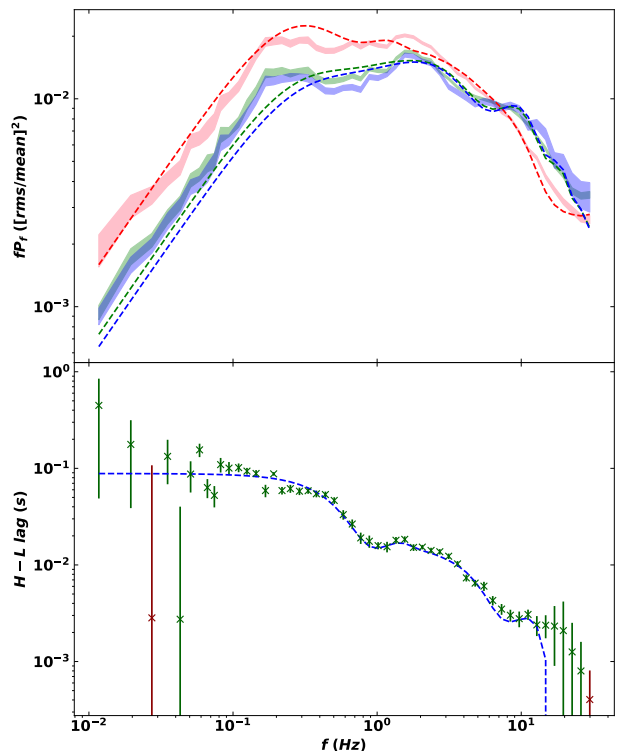


Figure 14. Timing fits using three component spectral fit *C*. Top panel (a): High, Mid & Low band PSDs. Colours as in Fig. 4(a). Bottom panel (b): High-Low band time lags. Colours and symbols as in Fig. 4(b). A time-domain animated version of this fit, including the effect on the spectral components and the mass fluctuation behaviour through the flow can be found at: youtu.be/bNGR5ws5lCg

emission. The main results of this study can be summarised as follows:

(i) The data require that the amount of turbulence per radial decade is neither constant, nor a smooth power-law function of radius. Instead annuli of enhanced turbulence are present, with regions of comparatively little variability separating them. These models therefore put less onus upon the MRI as the sole process driving the turbulence, as it is generally expected that the MRI will produce a uniform amount of variability per radial decade. The enhanced turbulence may instead be due to disc-flow interaction at the truncation radius, non-axisymmetric tilt shocks, flow-jet interaction, and/or other even less understood processes.

(ii) These regions of greater variability are also sometimes associated with additional emission. Unlike previous cases where the emission has been assumed to be a simple power-law function of radius (perhaps with an inner boundary condition), we find that the best fit cases require Compton-bright ‘rings’ in the hot flow. The variations in the light curve from these rings are accentuated relative to the rest of the flow, helping to give rise to the complex PSD structure.

(iii) The PSD hierarchy requires that some form of damping between spectral regions is included so that the lower energy bands see more low-frequency variability than the higher bands. This damping may be partly due to the im-

Spectral Model	<i>A</i>	<i>B</i>	<i>C</i>
	2 Comp.	2 Comp. (FR)	3 Comp. (FR)
PSDs, Lags	Fig. 4	Fig. 9	Fig. 14
$F_{var}(r)$, $\epsilon(r)$	Fig. 5	Fig. 10	Fig. 15
B_S	0.03(<i>F</i>)	0.03(<i>F</i>)	0.03(<i>F</i>)
m_S	0.5(<i>F</i>)	0.5(<i>F</i>)	0.5(<i>F</i>)
B_H	0.0184	0.679	n/a
m_H	2.35	0.309	n/a
B_{MH}	n/a	n/a	0.0385
m_{MH}	n/a	n/a	4.99×10^{-4}
r_o	13.4	16.4	14.3
r_i^\dagger	4.54	2.03	4.94
A_{en}^1	0.636	1.45	1.65
A_{en}^2	0.0649	0.588	3.96
A_{en}^3	3.80	1.57	0.0339
r_{en}^1	$= r_o$	$= r_o$	$= r_o$
r_{en}^2	12.0	5.21	8.48
r_{en}^3	5.05	2.26	4.98
σ_{en}^1	5.02	0.82	1.78
σ_{en}^2	1.34	5.74	0.141
σ_{en}^3	0.203	0.0208	1.36
Z_ϵ^2	9.09×10^8	1.86×10^6	214
Z_ϵ^3	7.71×10^8	6.25×10^9	79.3
γ	4.59	2.57	0.478
S_m^\ddagger	0.614	0.459	1.87×10^{-5}
D_{SH}	1.04	1.67	n/a
D_{SM}	n/a	n/a	1.41
D_{MH}	n/a	n/a	6.08
χ^2/dof	9617/295	3304/295	2788/294

[†]A hard limit of $r_i \geq 2$ (near the typical ISCO) is set for the inner radius of the hot flow.

[‡]A hard limit of $S_m \geq 0$ is set so that fluctuations do not unphysically become narrower as they propagate.

Table 5. Best-fitting parameter values for all timing models with a prior spectral fit shown in this work. We do not quote uncertainties due to the inherent parameter space degeneracies (discussed in Appendix C), and more importantly, the sensitivity to variation of the spectral model used as a prior.

pulse response of the mass fluctuation as it propagates, but is dominated by significant suppression of all fluctuation frequencies near the spectral transition radii.

(iv) Multiple continuum components showing correlated (but not identical) variability are required to produce distinct power spectra and non-zero time lags. A spectral decomposition consisting of two Compton components from distinct radial zones is sufficient to roughly approximate the shape and slope of the power spectra and lags respectively. To reproduce the complex lag step behaviour however, a spectral decomposition consisting of at least three Compton components within a stratified hot flow is required.

We regard these as fundamental features required in any model which can reproduce the spectra, PSDs and time lags, forming the basis for a new paradigm whereby the Compton emission is dominated by bright, turbulent rings in the inhomogeneous accretion flow. Beyond this basis, there are many

physical complexities which could be included to improve the fit quality. One could, for instance, include a low-frequency QPO signal. This QPO would have an unprecedentedly low quality factor if this effect is the source of any of the three power spectral peaks here, and its implementation would be inherently ad-hoc, particularly for its associated lag between bands. Phenomenological prescriptions have been tested before for the QPO (e.g. Ingram & Done 2012a), but the additional free parameters it would introduce are unattractive, particularly for a source such as Cygnus X-1 for which a clear QPO signal has never been recorded.

A different physical feature which would likely be of more interest in our case is spectral pivoting in the Hard component, driven by variations in the seed photon production from the Soft region. For spectral fit *B*, the position of the Hard seed photon temperature is quite close to the electron temperature of the Soft component ($kT_{seed,H} =$

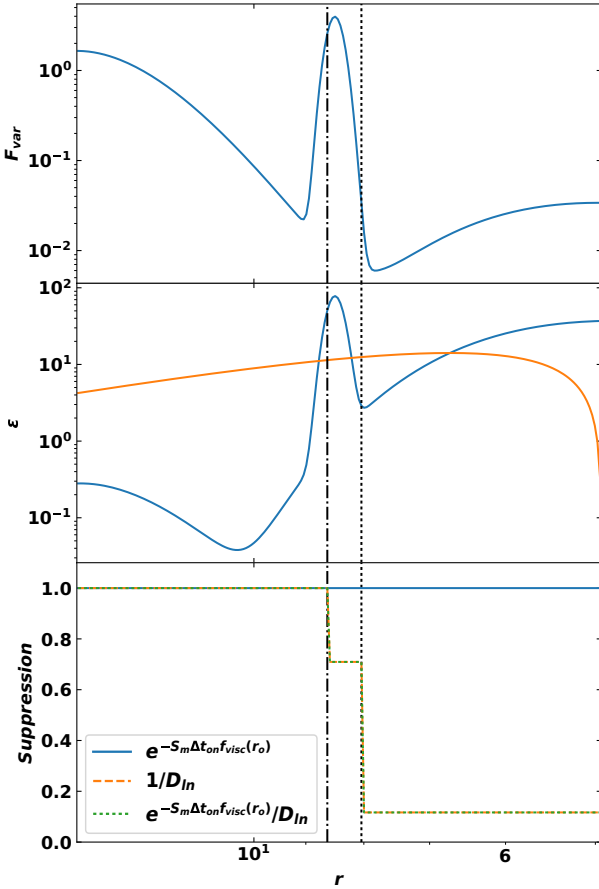


Figure 15. Fractional variability (F_{var} , top panel (a)), emissivity (ϵ , middle panel (b)) and smoothing/damping (bottom panel (c)) profiles found for fit of Fig. 14. Colours and linestyles as in Fig. 2.

3.05 ± 0.13 keV compared to $kT_{e,s} = 1.6 \pm 0.1$ keV), suggesting that at least some of the seed photons for the Hard component are from the Soft region. The variation in Soft region luminosity should therefore drive a change in the Hard component shape, and in turn should be an additional source of correlated variability between these components. This is of particular interest since our best fit case of Fig. 14 approximates the Hard and Mid band spectra well down to ~ 1 Hz, but cannot reproduce the low-frequency hump seen in these bands. Direct variability in the seed photons from the Soft component driving pivoting may help to correct this. If the Hard component pivot point is close to the High/Mid energy bands, pivoting would also result in variability suppression in the High/Mid bands relative to the Low band, relaxing the requirement for variability damping as m fluctuations propagate from the Soft to harder regions.

In future work, we will attempt to explore the effects of these model features, in addition to including a physically realistic reflection transfer function. We will also attempt to test this framework across the spectral transition in high signal-to-noise sources such as Cygnus X-1 and GX 339-4, to characterise the joint long-timescale evolution of the spectral components and the regions of enhanced emission/variability.

ACKNOWLEDGEMENTS

RDM and CD sincerely thank Magnus Axelsson for assistance with the Fourier-resolved spectral analysis and extensive discussions on the accretion flow behaviour. RDM acknowledges the support of a Science and Technology Facilities Council (STFC) studentship through grant ST/N50404X/1. CD acknowledges the STFC through grant ST/P000541/1 for support. This work used the DiRAC Data Centric system at Durham University, operated by the Institute for Computational Cosmology on behalf of the STFC DiRAC HPC Facility (www.dirac.ac.uk). This equipment was funded by BIS National E-infrastructure capital grant ST/K00042X/1, STFC capital grant ST/H008519/1, and STFC DiRAC Operations grant ST/K003267/1 and Durham University. DiRAC is part of the National E-Infrastructure. This research has made use of data obtained through the High Energy Astrophysics Science Archive Research Center Online Service, provided by the NASA/Goddard Space Flight Center.

SUPPORTING MATERIALS

A time-domain animated version of the timing fit using spectral model *C* can be found at: youtu.be/bNGR5ws5lCg. This video includes the mass accretion rate fluctuation behaviour through the flow, the effect on the spectral component variation, and the output time-domain light curves for a handy illustration of how the spectra and propagating fluctuations relate.

REFERENCES

- Arévalo P., Uttley P., 2006, MNRAS, 367, 801
 Arnaud K., Borkowski K.J., Harrington J.P., 1996, ApJ, 462, L75
 Axelsson M., Done C., 2018, <https://arxiv.org/abs/1803.01991>, Submitted to MNRAS
 Axelsson M., Hjalmarsdotter L., Borgonovo L. & Larsson S., 2008, A&A, 490, 253
 Balbus S.A., Hawley J.F., 1998, RvMP, 70, 1
 Basak R., Zdziarski A.A., 2016, MNRAS, 458, 2199
 Basak R., Zdziarski A.A., Parker M., Islam N., 2017, MNRAS, 472, 4220
 Blaes O., 2013, Space Sci. Rev., 103, 21
 Churazov E., Gilfanov M., Revnivtsev M., 2001, MNRAS, 321, 759
 Di Salvo T., Done C., Życki P.T., Burderi L., Robba N.R., 2001, ApJ, 547, 1024
 De Marco B., Ponti G., Muñoz-Darias T., Nandra K., 2015, ApJ, 814, 50
 Done C., Gierliński M., Kubota A., 2007, A&ARv, 15, 1 (DGK07)
 Esin A.A., McClintock J.E., Narayan R., 1997, ApJ, 489 (2), 865
 Foreman-Mackey D., Hogg D.W., Lang D., Goodman J., 2013, Publ. Astron. Soc. Pac, 125, 306
 Fragile P.C., Blaes O.M., Anninos P., Salmonson J.D., 2009, ApJ, 668, 417
 Gardner E., Done C., 2014, MNRAS, 442, 2456
 Genovozov A., Blaes O., Fragile P.C., Henisey K.B., 2014, ApJ, 780, 81
 Gierliński M., Zdziarski A.A., Done C. et al., 1997, MNRAS, 288, 958
 Gierliński M., Done C., Page K., MNRAS, 392, 1106
 Gilfanov M., Churazov E., Revnivtsev M., 2000, MNRAS, 316, 923

Grinberg V., Pottshmidt K., Böck M. et al., 2014, A&A, 565, A1
 Henisey K.B., Blaes O.M., Fragile P.C., 2012, ApJ, 761, 18
 Hogg J.D., Reynolds C.S., 2017, ApJ, 834, 80
 Ingram A., Done C., Fragile P.C., 2009, MNRAS, 397 (1), L101
 Ingram A., Done C., 2011, MNRAS, 415 (3), 2323 (ID11)
 Ingram A., Done C., 2012, MNRAS, 419, 2369
 Ingram A., Done C., 2012, MNRAS, 427, 934
 Ingram A., van der Klis M., 2013, MNRAS, 434, 1476 (IvdK13)
 Ingram A., van der Klis M., Middleton M. et al., 2016, MNRAS, 461 (2), 1967
 Kawano T., Done C., Yamada S., Takahashi H., Axelsson M., Fukuzawa Y., 2017, PASJ, 69(2), 36
 Klein-Wolt M., van der Klis M., 2008, ApJ, 675, 1407
 Kolehmainen M., Done C., Diaz Trigo M., 2014, MNRAS, 437, 613
 Kotov O., Churazov E., Gilfanov M., 2001, MNRAS, 327, 799
 Lubow S.H., Ogilvie G.I., Pringle J.E., 2002, MNRAS, 337, 706
 Lyubarskii Y.E., 1997, MNRAS, 292, 679
 Mahmoud R.D., Done C., 2017, MNRAS, 473, 2084 (MD17)
 Makishima K., Takahashi H., Yamada S. et al., 2008, PASJ, 60, 585
 Mastroserio G., Ingram A., van der Klis M., 2018, MNRAS, 475, 4027
 Misra R., Yadav J.S., Chauhan J.V. et al., 2017, ApJ, 835 (2), 195
 Miyamoto A., Kitamoto S., 1989, Nature, 342, 773
 Mushtukov A.A., Ingram A., van der Klis M., 2017, MNRAS, 474, 2259
 Narayan R., Yi I., 1995, ApJ, 452, 710
 Noble S.C., Krolik J.H., 2009, ApJ, 703, 964
 Nowak M.A., Vaughan B.A., Wilms J., Dove J.B., Begelman M.C., 1999, ApJ, 510, 874
 Nowak M.A., 2000, MNRAS, 318, 361
 Papadakis I.E., Lawrence A., 1993, MNRAS, 261, 612
 Pottshmidt K., Wilms J., Nowak M.A. et al., 2003, A&A, 407, 1039
 Rapisarda S., Ingram A., Kalamkar M., van der Klis M., 2016, MNRAS, 462, 4078
 Rapisarda S., Ingram A., van der Klis M., 2017, MNRAS, 469 (2), 2017 (R17a)
 Rapisarda S., Ingram A., van der Klis M., 2017, 472, 3821 (R17b)
 Shakura N.I., Sunyaev R.A., 1973, A&A, 24, 337
 Tomsick J.A. et al., 2014, ApJ, 780, 78
 Timmer J., König M., 1995, A&A, 300, 707
 Torii S., Yamada S., Makishima K. et al., 2011, PASJ, 63, S771
 Uttley P., Wilkinson T., Cassatella P., Wilms E., Pottshmidt K., Hanke M., Böck M., 2011, MNRAS, 414, L60
 Uttley P., Cackett E.M., Fabian A.C., Kara E., Wilkins D.R., 2014, Astron. Astrophys. Rev., 22, 72
 van der Klis M., 1989, in *Timing Neutron Stars: proceedings of the NATO Advanced Study Institute on Timing Neutron Stars*, p.27, Kluwer Academic / Plenum Publishers, ed. Ögelman H. & van den Heuvel E.P.J.
 Veledina A., 2016, ApJ, 832, 181
 Wijnands R., van der Klis M., 1999, ApJ, 522 (2), 965
 Wilkinson T., Uttley P., 2009, MNRAS, 397, 666
 Wilms J., Allen A., McCray R. 2000, ApJ, 542, 914
 Yamada S., Makishima K., Done C., Torii S., Noda H., Sakurai S., 2013, PASJ, 65, 80
 Zdziarski A.A., Johnson W.N., Magdziarz P., 1996, MNRAS, 283, 193

APPENDIX A: TIMING FORMALISM FOR TWO SPECTRAL COMPONENTS

IvdK13 show that in the absence of damping, the propagated mass accretion rate curve at a given annulus can be written as:

$$\dot{M}(r_n, t) = \prod_{l=1}^n \dot{M}(r_l, t - \Delta t_{ln}), \quad (\text{A1})$$

where we denote capital $\dot{M}(r_n, t)$ as the *propagated* mass accretion rate at radius r_n , distinct from the generated variability at r_n , $\dot{m}(r_n, t)$. This of course implies that $\dot{M}(r_o, t) = \dot{m}(r_o, t)$.

However recent work (R17a, Mushtukov, Ingram & van der Klis 2017) has highlighted that equation (A1) is only a specific case of the Green's function for the accretion of an annular unit mass from radius r_l to r_n , $G(r_l, r_n, t)$. This function describes how a delta function perturbation initialised at r_l spreads and propagates toward the compact object, to be observed at some inner annulus r_n . The general case of the generator functions is therefore given by

$$\dot{M}(r_n, t) = \prod_{l=1}^n G(r_l, r_n, t) \otimes \dot{M}(r_l, t), \quad (\text{A2})$$

where \otimes denotes a convolution. In the case where $G(r_l, r_n, t) = \delta(t - t_{ln})$, we recover equation (A1) and the power spectrum of mass accretion rate fluctuations becomes the standard case of IvdK13,

$$|\tilde{M}(r_n, f)|^2 = |\tilde{m}(r_n, f)|^2 \otimes |e^{2\pi i \Delta t_{(n-1)n} f} \tilde{M}(r_{n-1}, f)|^2. \quad (\text{A3})$$

In reality, an infinitely narrow annulus propagating according to equation (A3) would be unphysical, as it would simply move toward the black hole without dispersing radially. Instead, as the surface density fluctuations propagate, they are also expected to smooth out. For a radiatively inefficient accretion flow, the relation between the smoothing timescale and the local viscous timescale is poorly understood, so we follow R17a in parameterising the Fourier transform of this part of the Green's function as an exponential decay with frequency and lag time, scaled by the smoothing parameter, S_m . This prescription has the property of smoothing out older and/or shorter timescale fluctuations first, as we would expect a physically realistic accretion flow to do.

In MD17 we also showed that the Low-band dominance of the PSDs at low frequencies demands that the seed photon variability from $r > r_{SH}$ be suppressed on propagation into the inner regions. Such seed photon suppression may arise from clump evaporation as thermal packets torn from the disc dissipate as they are accreted. We again model this generically by only including a fraction D_{SH}^{-1} of the low frequency noise propagated from the outer regions in the time series of the inner regions. The effect of this damping is distinct from the diffusive smoothing process, in that it affects all fluctuations equally irrespective of frequency or of lifetime within the flow. This prescription is only the simplest possible way to include damping, where the suppression of amplitude takes place at a specific radius. It could instead be a continuous function of radius, but since the final band-dependent light curves are simply weighted sums of the *average* mass accretion rates in each spectral region, the discrete and continuous suppression cases are interchangeable in the model. The final Green's function therefore has

a Fourier transform of

$$\tilde{G}(r_l, r_n, f) = \frac{1}{D_{ln}} e^{2\pi i \Delta t_{ln} f} e^{-S_m \Delta t_{ln} f}, \quad (\text{A4})$$

where the damping parameter D_{ln} is described by

$$D_{ln} = \begin{cases} D_{SH} & \text{if } r_l < r_{SH} < r_n \\ 1 & \text{otherwise.} \end{cases} \quad (\text{A5})$$

The propagated PSDs are now described by

$$|\tilde{M}(r_n, f)|^2 = |\tilde{m}(r_n, f)|^2 \otimes |\tilde{G}(r_{n-1}, r_n, f) \tilde{M}(r_{n-1}, f)|^2, \quad (\text{A6})$$

which shows that the mass accretion rate in each annulus is simply a sequential convolution of all those preceding it (rescaled by their Green's functions). The modified equation in terms of the input generator power spectra is therefore

$$|\tilde{M}(r_n, f)|^2 = \prod_{l=1}^n \left| e^{-S_m \Delta t_{ln} f} \frac{\tilde{m}(r_l, f)}{D_{ln}} \right|^2, \quad (\text{A7})$$

where the coproduct symbol denotes sequential convolutions.

Our mass accretion rates are converted to counts in a given band using the emissivity prescription and SED decomposition described in Section 2.3. This effectively weights the propagated mass accretion rate from each annulus by a factor, w_n^{band} , given by

$$w_n^{band}(r_n) = \frac{\epsilon(r_n) r_n dr_n}{\sum_{region} \epsilon(r_n) r_n dr_n} \int_{E=E_{band}^{min}}^{E_{band}^{max}} \tilde{F}(E, r_n) A_{eff}(E) e^{-N_H(E) \sigma_T} dE, \quad (\text{A8})$$

where $A_{eff}(E)$ is the detector effective area, $N_H(E)$ is the galactic column absorption and σ_T is the Thompson cross-section. The count spectrum for that band can then be written

$$C_{band}(t) = \sum_{n=1}^N w_n^{band} \dot{M}(r_n, t). \quad (\text{A9})$$

Since the mean count rate of $\dot{M}(r_n, t)$ is normalised to \dot{M}_0 , the mean count rate in a given energy band is then

$$\mu_C = \sum_{n=1}^N \dot{M}_0 w_n^{band}. \quad (\text{A10})$$

Dropping the superscript on w_n^{band} , the rms-normalised power spectrum of the variability in this energy band is then

$$\begin{aligned} P_{band}(f) &= \frac{2dt^2}{\mu_C^2 T} |\tilde{C}_{band}(f)|^2 \\ &= \frac{2dt^2}{\mu_C^2 T} \sum_{l,n=1}^N w_n w_l \tilde{M}(r_l, f)^* \tilde{M}(r_n, f). \end{aligned} \quad (\text{A11})$$

Since our Green's function has the property $G(r_l, r_n, t) = G(r_l, r_k, t) \otimes G(r_k, r_n, t)$, or equivalently $\tilde{G}(r_l, r_n, f) = \tilde{G}(r_l, r_k, f) \tilde{G}(r_k, r_n, f)$, we can use the same arguments as the case of the Green's function of IvdK13 to show that, in the case of unity mean mass accretion rate at each annulus, the cross-spectrum between annuli can be expressed,

$$\tilde{M}(r_l, f)^* \tilde{M}(r_n, f) = \frac{e^{2\pi i \Delta t_{ln} f} e^{-S_m \Delta t_{ln} f}}{D_{ln}} |\tilde{M}(r_l, f)|^2. \quad (\text{A12})$$

The band-dependent power spectrum therefore becomes

$$\begin{aligned} P_{band}(f) &= \frac{2dt^2}{\mu_C^2 T} \sum_{n=1}^N [w_n^2 |\tilde{M}(r_l, f)|^2 \\ &\quad + 2 \sum_{l=1}^{n-1} w_l w_n \cos(2\pi \Delta t_{ln} f) \frac{|\tilde{M}(r_l, f)|^2}{e^{S_m \Delta t_{ln} f} D_{ln}}]. \end{aligned} \quad (\text{A13})$$

We can also compare the power spectra in different energy bands

$$\Gamma_{LH}(f) = \frac{2dt^2}{\mu_L \mu_H T} \tilde{C}_L(f)^* \tilde{C}_H(f), \quad (\text{A14})$$

which yields a result for the cross-spectrum analogous to that of equation (A13),

$$\begin{aligned} \Gamma_{LH}(f) &= \frac{2dt^2}{\mu_L \mu_H T} \sum_{n=1}^N [w_n^L w_n^H |\tilde{M}(r_l, f)|^2 \\ &\quad + \sum_{l=1}^{n-1} (w_l^L w_n^H e^{2\pi i \Delta t_{ln} f} + w_l^H w_n^L e^{-2\pi i \Delta t_{ln} f}) \frac{|\tilde{M}(r_l, f)|^2}{e^{S_m \Delta t_{ln} f} D_{ln}}]. \end{aligned} \quad (\text{A15})$$

Phase/time lags can then be obtained by splitting this cross spectrum into its real and imaginary parts,

$$\begin{aligned} \Re[\Gamma_{LH}(f)] &= \frac{2dt^2}{\mu_L \mu_H T} \sum_{n=1}^N [w_n^L w_n^H |\tilde{M}(r_l, f)|^2 \\ &\quad + \sum_{l=1}^{n-1} \cos(2\pi \Delta t_{ln} f) (w_l^L w_n^H + w_l^H w_n^L) \frac{|\tilde{M}(r_l, f)|^2}{e^{S_m \Delta t_{ln} f} D_{ln}}], \end{aligned} \quad (\text{A16})$$

$$\begin{aligned} \Im[\Gamma_{LH}(f)] &= \frac{2dt^2}{\mu_L \mu_H T} \sum_{n=1}^N \sum_{l=1}^{n-1} [(w_l^L w_n^H - w_l^H w_n^L) \\ &\quad \times \sin(2\pi \Delta t_{ln} f) \frac{|\tilde{M}(r_l, f)|^2}{e^{S_m \Delta t_{ln} f} D_{ln}}]. \end{aligned} \quad (\text{A17})$$

From these complex components, the time lag is then extracted as

$$\tan(2\pi f \tau_{LH}) = \frac{\Im[\Gamma_{LH}(f)]}{\Re[\Gamma_{LH}(f)]}, \quad (\text{A18})$$

in the same way as the observed timing statistic, which allows direct comparison to the data.

APPENDIX B: A DEVELOPED PHYSICAL PICTURE FOR THE OBSERVED TIME LAGS

In MD17, we demonstrated how the maximal time lag - that for the lowest frequencies generated at r_o - can be understood in terms of fluctuations propagating from the characteristic Soft to the characteristic Hard position, $\langle r_S \rangle$ and $\langle r_H \rangle$. These are simply the emissivity weighted average positions within each region,

$$\langle r_S \rangle = \frac{\int_{r_{SH}}^{r_o} r^2 \epsilon(r) dr}{\int_{r_{SH}}^{r_o} r \epsilon(r) dr}, \quad \langle r_H \rangle = \frac{\int_{r_l}^{r_{SH}} r^2 \epsilon(r) dr}{\int_{r_l}^{r_{SH}} r \epsilon(r) dr}. \quad (\text{B1})$$

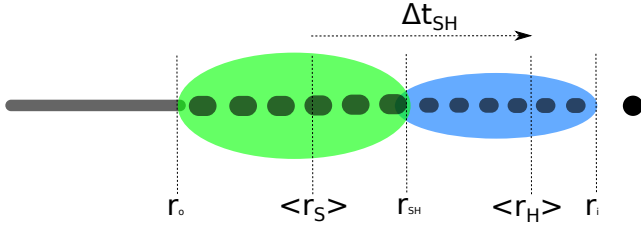


Figure B1. Simplified picture of the lag origin in the two Compton component model. Colours as in Fig 1.

The maximum raw lag is then the propagation time between these radii

$$\Delta t_{SH} = \int_{\langle r_H \rangle}^{\langle r_S \rangle} \frac{dr}{r f_{\text{visc}}(r)} \quad (\text{B2})$$

$$= \frac{2\pi R_g}{Bc} \left[\frac{\langle r_S \rangle^{m+3/2}}{m+3/2} - \frac{\langle r_H \rangle^{m+3/2}}{m+3/2} + \frac{\langle r_S \rangle^m}{m} - \frac{\langle r_H \rangle^m}{m} \right].$$

This raw lag is illustrated schematically in Fig. B1. The lag we measure is then diluted due to the overlap of the Soft spectral component into the High band and the Hard component into the Low band (Uttley et al. 2014), yielding

$$\tan[2\pi f_o \tau_{\text{dil}}] = \frac{\sin(2\pi f_o \Delta t_{SH})(F_{\text{Soft}}^L F_{\text{Hard}}^H - F_{\text{Soft}}^H F_{\text{Hard}}^L)}{F_{\text{Soft}}^L F_{\text{Soft}}^H + F_{\text{Hard}}^L F_{\text{Hard}}^H + \cos(2\pi f_o \Delta t_{SH})[F_{\text{Soft}}^L F_{\text{Hard}}^H + F_{\text{Soft}}^H F_{\text{Hard}}^L]}, \quad (\text{B3})$$

where F_i^j is the total flux due to spectral component i in band j . For sufficiently ‘peaked’ emissivity profiles, (i.e. the emission profile is approximately delta functions at $\langle r_S \rangle$ and $\langle r_H \rangle$ and negligible elsewhere), f_o can be replaced with f , generalising equation (B3) to all frequencies. Introducing the Soft-Hard damping mechanism, frequencies $f < f_{\text{visc}}(r_{SH})$ are also suppressed by a factor D_{SH} in the Hard region relative to the Soft, and so we arrive at a modified form for the final measured lag,

$$\tan[2\pi f \tau_{\text{fin}}(f)] = \frac{\sin(2\pi f \Delta t_{SH})(F_{\text{Soft}}^L F_{\text{Hard}}^H - F_{\text{Soft}}^H F_{\text{Hard}}^L)}{D_{SH} F_{\text{Soft}}^L F_{\text{Soft}}^H + F_{\text{Hard}}^L F_{\text{Hard}}^H + \cos(2\pi f \Delta t_{SH})[F_{\text{Soft}}^L F_{\text{Hard}}^H + F_{\text{Soft}}^H F_{\text{Hard}}^L]}.$$

Equation (B4) holds well at low frequencies in all cases, with only minor discrepancies introduced by the width of the Fourier-space generator Lorentzians away from $\langle r_S \rangle$ and $\langle r_H \rangle$. For peaked emissivities, the lags at other frequencies are also consistent with equation (B4). In Fig. B2 we demonstrate this by comparing the lags of equation (B4) with the rigorous prediction of equation (A18) for delta function emissivities at arbitrary $\langle r_S \rangle$ and $\langle r_H \rangle$. We note that the models agree remarkably well, showing that lag terms of higher order than equation (B4) can be ignored in the case of this very simple emissivity.

However for broader emission profiles, the lag can significantly diverge from the equation (A18) prediction, since this breaks the key assumption in equation (B2) of the emission being dominated by $\langle r_S \rangle$ and $\langle r_H \rangle$. Ultimately the continuum of emission leads to a greater contribution from the lags associated with other annuli and cross-term interference, and equation (B4) breaks down. The broader

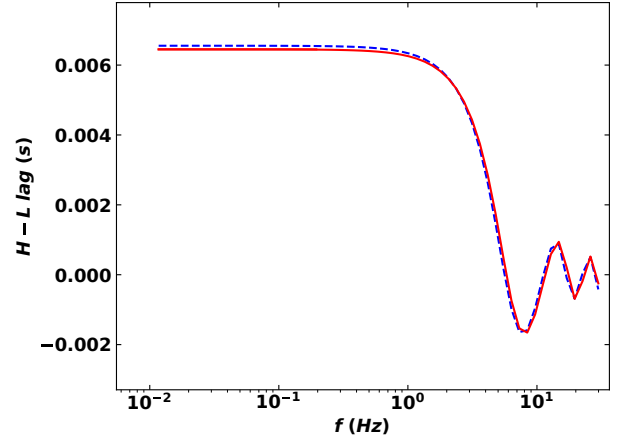


Figure B2. Comparison of lags predicted by the analytic model adapted from IvdK13 (equation A18, blue dashed line) and the physically-motivated lag model of equation (B4) (red solid line) for simple delta function emissivities at arbitrary $\langle r_S \rangle$ and $\langle r_H \rangle$. Here we use an arbitrarily selected $D_{SH} = 3$, viscosity parameters of $B = 0.03$ and $m = 0.5$ and spectral contributions to the Low and High bands from Fig. 3.

the emission profile, the more this physically simplified result diverges from the complex analytic prediction of equations (A14)-(A18).

APPENDIX C: UNCERTAINTIES ON FIT PARAMETERS

Due to its sheer size, the parameter space formed by the final model in this work suffers from some inherent degeneracy. Several of the posterior distributions obtained for these parameters from the MCMC chains were therefore non-gaussian. Partly for this reason we do not quote parameters with errors, but instead show an example corner plot of the posterior distributions for a spectral-timing fit in Fig. C1. This figure shows the posterior distributions for all pairs of parameters for the fit of Fig. 14. A good example of the ‘banana’ structure characteristic of degeneracy can be seen in the γ - Z_ϵ^1 or γ - Z_ϵ^2 distributions in Fig. C1. This is clearly because the parameters γ , Z_ϵ^1 and Z_ϵ^2 could be dependently varied to form similar $\epsilon(r)$ profiles. By contrast, the damping parameters of D_{SM} and D_{MH} are quite independent of other parameters and could be well determined for a given spectral prior variant. However, even when parameters are well constrained and non-degenerate in the timing fits, these parameters are highly sensitive to the spectral fit used as a prior, and so may vary dramatically for alternative spectral fits.

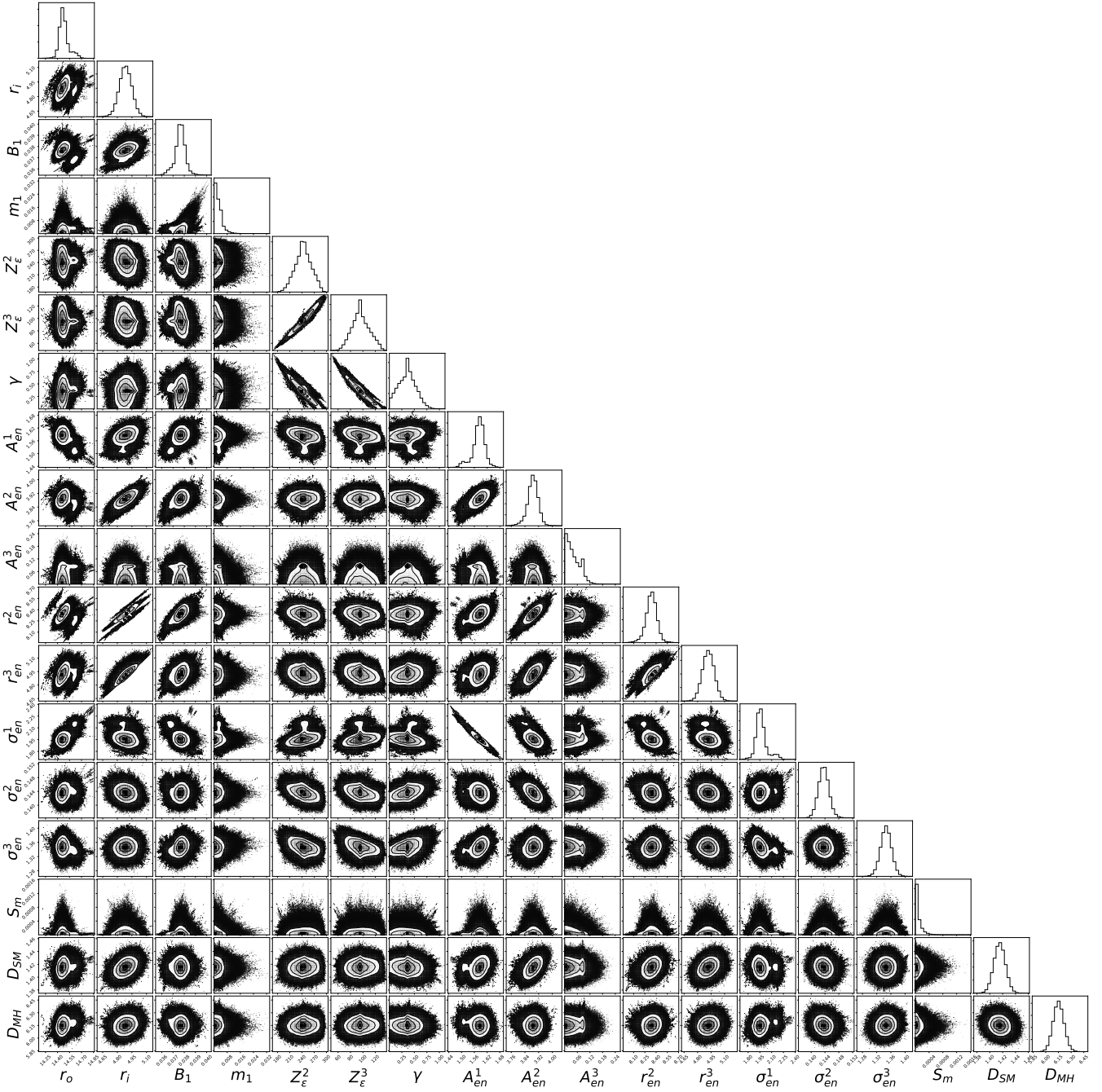


Figure C1. Posterior probability distributions found from the MCMC fit of Fig. 14, shown as an example of the parameter space degeneracies. Interior contour plots show the optimal regions of parameter space for all pairs of parameters. Panels at the top of each column show the 1-dimensional posterior distributions of each parameter, integrated over all other parameters. Note that this plot is best viewed digitally to avoid pixelization of the contours.

This paper has been typeset from a \LaTeX file prepared by the author.